The Thesis Committee for Laura Homiller
certifies that this is the approved version of the following thesis:

Self-Sensing Hysteresis-Type Bearingless Motor

APPROVED BY

SUPERVISING COMMITTEE:

Lei Zhou, Supervisor

Raul Longoria

Self-Sensing Hysteresis-Type Bearingless Motor

by

Laura Homiller

Thesis

Presented to the Faculty of the Graduate School of

The University of Texas at Austin

in Partial Fulfillment

of the Requirements

for the Degree of

Master of Science in Engineering

The University of Texas at Austin

May 2022

For my family.

Acknowledgments

First I would like to thank Dr. Lei Zhou for supporting this work. I have so appreciated her support, patience, and guidance throughout this project, and am very grateful to be able to work with and learn from her.

There are so many people who have supported me through this project. I'm grateful for my labmates and the suggestions and input they've provided. I would especially like to thank Ian Heyman for all his help with building the system and for his patience with me in the machine shop. My dear roommates have been an invaluable support; I'm so grateful for their friendship and for all the good and bad moments we've gotten to share. And of course I would like to thank my family for being a constant in my life, and for being so supportive not only through this project, but through everything up to this point.

Laura Homiller

The University of Texas at Austin
May 2022

Abstract

Self-Sensing Hysteresis-Type Bearingless Motor

Laura Homiller, M.S.E.
The University of Texas at Austin, 2022

Supervisor: Lei Zhou

This thesis presents the design, implementation, control, and experimental evaluation of a self-sensing hysteresis-type bearingless motor (SSBM). Bearingless motors are well-suited to high-speed applications due to their frictionless operation, but the magnetic levitation of the rotor is unstable without airgap sensors. Eliminating these sensors decreases system cost and volume while increasing system robustness. This work presents the design for a hysteresis-type bearingless motor that operates without the use of airgap sensors.

Bearingless motors use a single stator to generate torque and suspension forces to control the position of the rotor. Some measure of the airgap length is needed to enable stable magnetic suspension, so this thesis proposes the injection of a high-frequency carrier signal to the stator windings to amplify the change in coil inductance with rotor position. The coil response is demodulated against the

carrier signal to provide an estimate for airgap length.

This design uses a stator with 12 independently controlled windings to generate a 4-pole magnetic field for torque and a 2-pole magnetic field to control the rotor suspension. Analytical and finite-element simulation demonstrate that if the current in the windings is controlled, demodulating the winding voltage against the carrier signal gives a good estimate for rotor displacement. When the winding voltage is considered the input, the current through the coils can be used for estimation, but the result is highly dependent on the suspension field.

The prototype developed to test this operating principle has been constructed and tested with voltage as the winding input. Inductive sensors are used to provide a "ground truth" signal to evaluate the estimation result and to provide feedback for the rotor suspension while the estimation is being developed. Initial results show that even under voltage control the SSBM prototype is able to estimate the rotor displacement, but only when the suspension control is active. Current control for the system has been developed and will be implemented as the immediate next steps.

Table of Contents

List of Tables

List of Figures

Chapter 1

Thesis Overview

This thesis develops a method to estimate the airgap in a bearingless hysteresis motor using the electrical response of the stator windings in order to enable magnetic levitation of the rotor without the need for external sensors. This chapter presents an overview of the work that has been completed so far on the development of the self-sensing bearingless motor (SSBM) and the key results.

Bearingless motors are electric machines that generate torque and magnetic suspension forces using a single stator assembly, enabling non-contact and maintenance free operation. The magnetic suspension of the rotor is inherently unstable, so feedback of the rotor position is typically accomplished using costly airgap sensors. The objective of this project is to accomplish the suspension feedback for the bearingless motor without external sensors, instead using a high frequency carrier signal to enable the estimation of airgap length based on the electrical response of the stator coils.

1.1 1-DOF airgap estimation and analytical modeling of self-sensing bearingless motor

The key idea for the airgap estimation is the injection of a high-frequency carrier signal to amplify the effect of the changing inductance due to variable airgap length on the winding voltage. To establish the basis for this self-sensing approach, a 1-DOF E-core system was tested, shown in Figure 1.1. The airgap length between the E-core stator and upper bar was varied using plastic shims. The current input to the coil had a 60 Hz component analogous to the motor current in the full system, and a 2 kHz component to enable the airgap estimation. When the coil voltage was demodulated against the 2 kHz carrier signal, the results gave a clear relationship between airgap length and coil voltage, summarized in Figure 1.2.

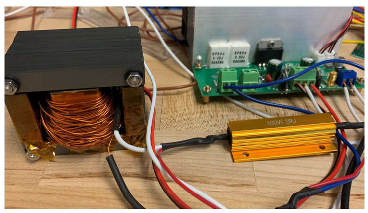

(a) 1-DOF maglev system photo.

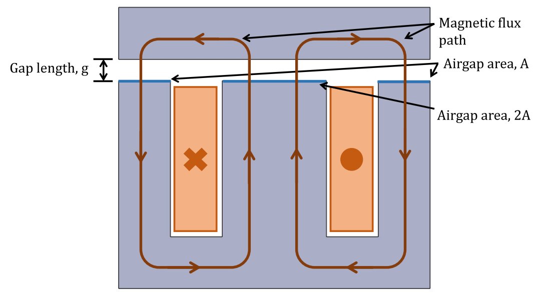

(b) 1-DOF maglev system flux path.

Figure 1.1: 1-DOF E-core magnetic levitation system

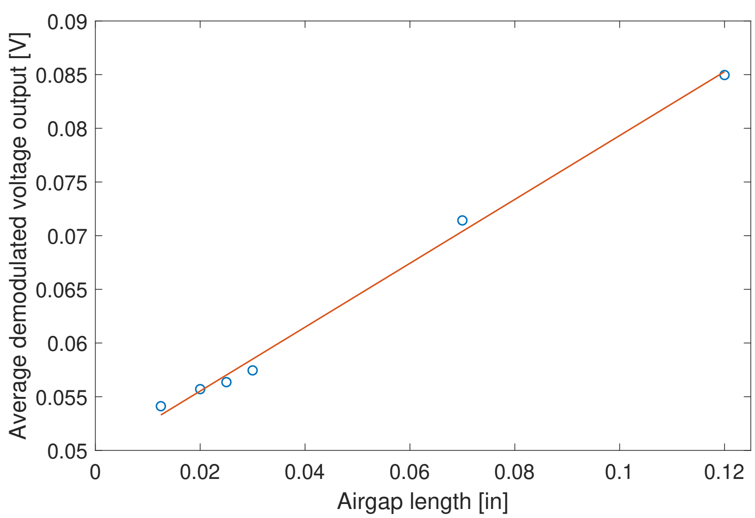

Figure 1.2: 1-DOF example maglev system sampled airgap length demodulation results.

An analytical model for the full bearingless motor was derived and used to simulate the estimation of the airgap for two cases. First, the current was considered as the input to the coils and the voltage response was used to estimate the airgap. This approach demonstrated a clear correlation between the estimation signal and the actual airgap length, shown in Figure 1.3a. The simulation was then repeated for the system under voltage control, where voltage is input to the coils and the current is measured and used for the airgap estimation. The results of this simulation are given in Figure 1.3b. Based on the analytical model for the bearingless motor, airgap estimation using this method is possible using either voltage or current control, but a much larger amplitude is needed for the carrier signal under voltage control.

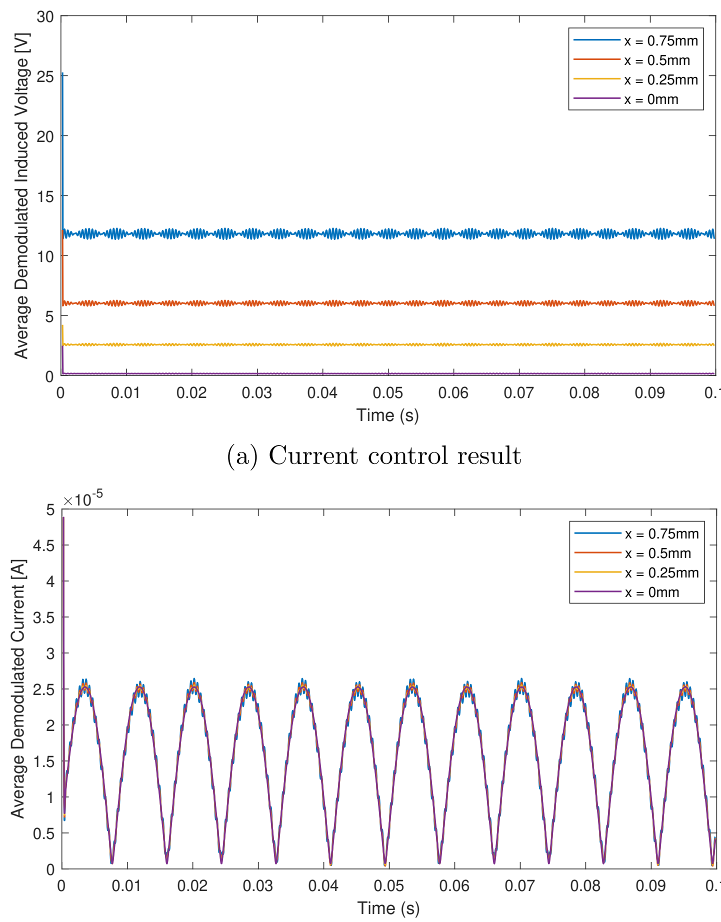

(a) Current control result

(b) Voltage control result

Figure 1.3: Results from simulations using an analytical model of the SSBM

1.2 Hardware design

Having established the potential for this approach, a testbed was designed for experimental evaluation. The constructed prototype is shown in Figure 1.4. This design includes four inductive sensors as a "ground truth" against which the estimation method is evaluated. A D2 tool steel rotor is supported by a shaft which is constrained at one point at the bottom of the assembly by a tooling ball in a cone-shaped mounting plate. This allows the rotor to move in x, y, and θ_z DOFs while constraining motion in all other DOFs. The radial displacements of the rotor are actively controlled by a 2-pole magnetic field generated by the stator coils, and torque is generated through the interaction of a 4-pole magnetic field and the hysteresis effect of the rotor material. The 12 stator coils are each individually controlled, and the input commands are designed such that both the 2-pole field for suspension and 4-pole field for rotation are generated by the single set of windings.

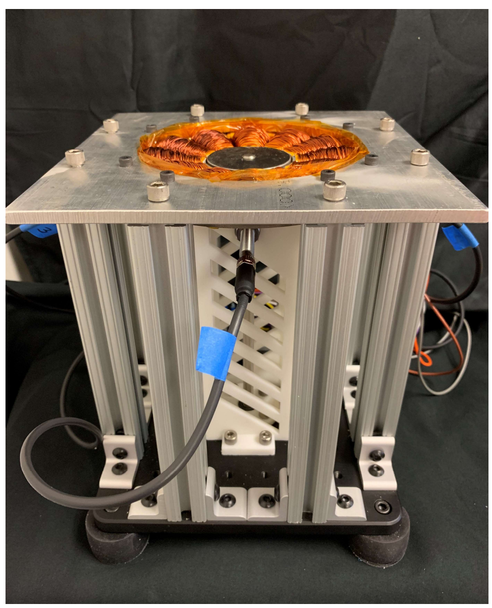

Figure 1.4: Photograph of SSBM assembly.

1.3 Control and airgap estimation implementation

Figure 1.5 shows the control block diagram for the bearingless motor, where currents are input to the stator windings and the voltage response is demodulated against the high-frequency carrier signal for airgap estimation. The digital portion of the control and airgap estimation was implemented in LabVIEW on a cRIO-9048.

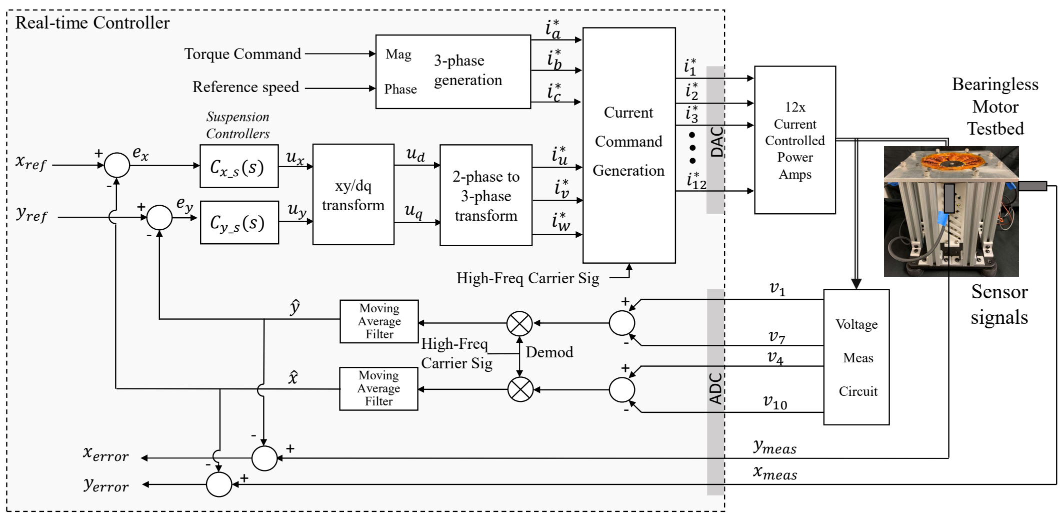

Figure 1.5: Self-sensing bearingless motor control block diagram.

A printed circuit board (PCB) for analog current control has been developed, and will be used to test the SSBM prototype under current control. For voltage control, the above block diagram is modified such that the voltages of the coils are supplied and the current signals are measured with power resistors in series with the stator windings. Linear power amplifiers were used to amplify the command signals from the real-time controller.

1.4 FEM simulation and experimental evaluation

The proposed SSBM system was modeled in ANSYS Maxwell with both current and voltage as the input to the coils. In a similar way to the results from the analytical modeling, the estimation result from the FEM simulation under current control provided good differentiation for various rotor displacements, shown in Figure 1.6. The simulation under voltage control did not give good results when demodulated against the 2 kHz carrier signal, but when the current output was demodulated against a 120 Hz signal the estimation result was much improved, shown in Figure 1.7. This is due to the inductive nature of the coils, where the magnitude of the frequency response drops off at high frequencies. The result at 120 Hz comes from the interaction of the 60 Hz suspension and rotation fields, which are able to modulate the rotor displacement signal at 120 Hz.

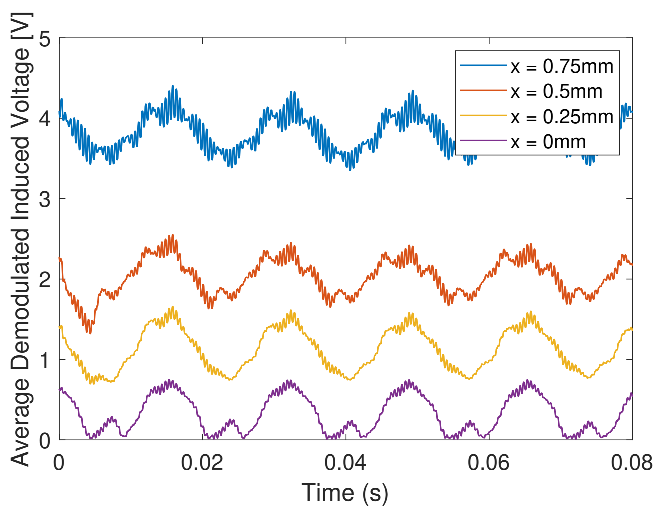

Figure 1.6: FEM estimation results under current control

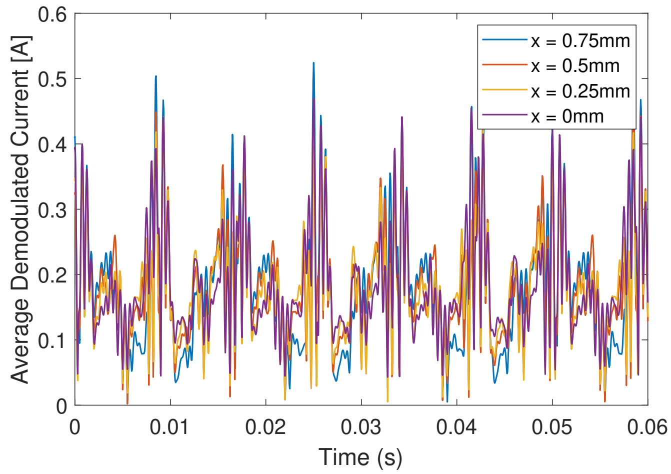

(a) Coil currents demodulated at 2 kHz

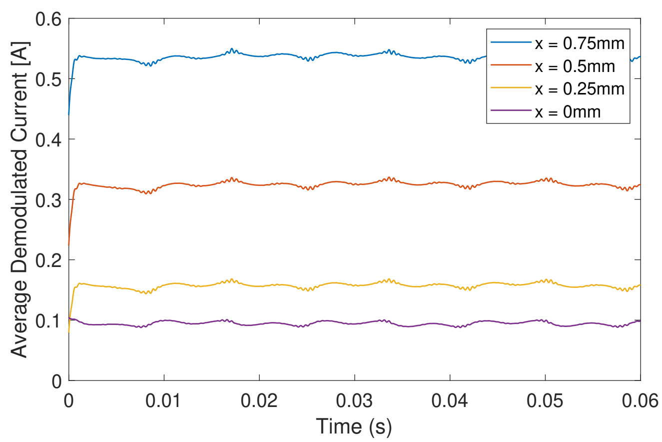

(b) Coil currents demodulated at 120 Hz

Figure 1.7: Results of FEM simulation under voltage control

The proposed estimation approach was then tested on the constructed SSBM prototype. Figure 1.8 shows the result of the airgap estimation for manual disturbance of the rotor in both the x- and y- directions. Once the demodulated signal is scaled to give a value in mm, the result closely matches the position readings of the inductive sensors. While under voltage control the estimation only works when the suspension and rotation fields are active, suggesting that the injected carrier signal is too small to enable estimation on its own. Even so, some interaction of the suspension and rotation fields does provide a good estimate for rotor displacement. Hardware delays have resulted in the current control testing being pushed to future work, so only voltage control results are presented in this thesis. It is expected that the estimation performance will improve once current control is implemented, based on the simulation results.

The rest of this thesis is organized as follows. Chapter 2 discusses the motivation and prior art for bearingless motors and self-sensing levitation. Chapter 3 presents the analytical model for the SSBM and simulation results for both current and voltage commands. Chapter 4 details the hardware implementation for the SSBM prototype developed to test the presented estimation technique. Chapter 5 discusses the suspension control system and the estimation method that enables self-sensing operation of the motor prototype. Chapter 6 presents the both the results of FE simulation of the SSBM system and initial results of experimental testing of the SSBM prototype with voltage commands. Chapter 7 concludes the work and presents suggestions for future work.

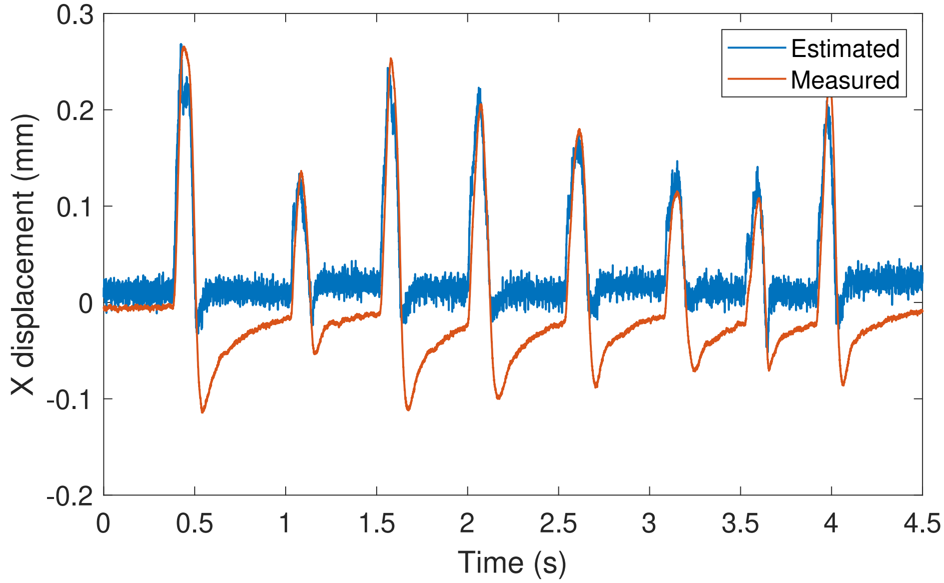

(a) X-direction displacement

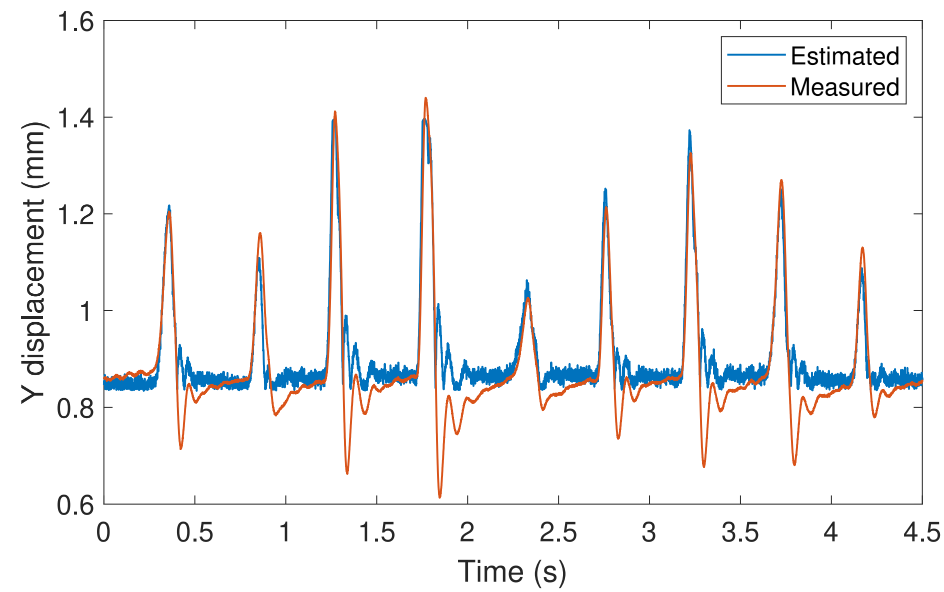

(b) Y-direction displacement

Figure 1.8: Estimator response to manual disturbance

Chapter 2

Background and Motivation

2.1 Motivation

The development of high-speed electric machines is attracting increasing research for a wide range of promising applications including electric transportation and portable power storage. Increasing the speed of a machine enables an equivalent power output at a reduced weight and volume, making high-speed operation a highly desirable capability for applications which require a compact design such as small liquid pumps [1], or those that require high-speeds like optical scanning devices [2].

Bearingless motors are an emerging technology that is particularly well-suited to high-speed applications. In a bearingless motor, a single stator assembly produces both torque and levitation forces on the rotor, which requires reduced shaft length and rotor inertia than machines that use separate magnetic bearings. Because the rotor is magnetically levitated, these machines operate without bearing friction, enabling them to operate for a nearly unlimited lifetime without maintenance. This feature is highly desirable for high-speed applications, because mechanical bearings faults are a common point of failure in those motors. Another significant benefit of non-contact operation is the ability of the system to operate in a vacuum environment, or to be used in pump applications where lubricant contamination is unacceptable.

As with other magnetically levitated systems, bearingless motors require closed-loop feedback control to enable stable levitation of the rotor. This requires the measurement and feedback of the airgap length, which is typically accomplished using inductive, capacitance, or eddy current sensors [3]. However, the inclusion of the sensors adds significant cost, decreases the overall system robustness in harsh environments, and increases the system volume. Therefore, it is highly desirable to create a new type of bearingless motors without the need for costly airgap sensors, thereby enabling new high-speed machines that are simultaneously high performance, maintenance-free, and low cost for various applications.

2.2 Prior art

Prior study on this topic has primarily focused on either the bearingless operation of a motor, or on the implemention of self-sensing techniques in magnetic bearings, with only a few examples of self-sensing bearingless motors existing. This section provides a review of relevant literature on both bearingless motors and self-sensing magnetic bearings.

2.2.1 Bearingless motors

Today's bearingless motor technology largely exists in the research space with only a few examples of industry application such as the bearingless pumps developed by Levatronix Inc. (levatronix.com) [4]. The most common types of bearingless motors in the literature use permanent magnet synchronous motors (PMSM) or induction machines (IM) for the torque generation, but nearly all types of motors have been studied within this field [3].

The most common type of bearingless motor is permanent magnet synchronous machines, owing to their advantages of high efficiency and high torque density [5]. An early analysis of these machines is given in [6], and various configurations of these machines are given in [4,5,7,8]. It was demonstrated in [9] that the torque and suspension force control in a bearingless PMSM are independent, which significantly simplifies the control strategy for these machines.

Induction-type motors are the most widely used motor type in industry for their low cost and robustness. Bearingless induction motors of various configurations have been studied in [10–13]. These machines typically do not achieve the same efficiency or power rating as typical industrial induction motors [3]. One of the reasons for low efficiency in bearingless IMs is the current induced in the rotor by the suspension fields. In a recent study [12], the optimal design of these machines is investigated, and a model for high efficiency design is proposed. This design has improved the motor's efficiencies to the range of 95%. Up to this point, most bearingless IMs are used for low power applications such as the blood pump in [13]. As efficiencies improve more opportunities for industrial application will evolve [14].

Hysteresis motors use the magnetic hysteresis effect of the rotor material to generate torque. The rotor in these machines is a solid piece of magnetically semi-hard material, meaning that no permanent magnets or rotor windings are needed. This makes the rotors extremely high strength, which is advantageous for high-speed operation. In addition, the absence of permanent magnets means that demagnetization and magnet temperature constraints are not a concern, making hysteresis motors desirable for extreme temperature environments. Bearingless hysteresis motors have been studied in [15] and [16].

Other bearingless motor types that have been investigated include reluctance motors [17,18], ac homopolar [19], and flux-switching permanent magnet motors [20].

A major challenge for more widespread use of bearingless motors is their need for closed-loop feedback for suspension control. This is typically accomplished through the inclusion of airgap sensors, the most common varieties being inductive, capacitive, or eddy current sensors [3]. These sensors increase the cost and volume of the system and cannot be used in harsh environments. Eliminating the need for airgap sensors is a key step to improving existing bearingless motor technologies.

2.2.2 Self-sensing magnetic bearings and bearingless motors

Active magnetic bearings (AMB) have been used in industry for a number of years after first being developed in the 1980s. As an alternative to mechanical bearings, AMBs provide the benefits of magnetic suspension as a modular addition to traditional motors. Because gap sensors are costly, there have been efforts to operate the feedback loop without these sensors. It has been demonstrated that an AMB with voltage-controlled windings is fully observable, so linear observers can use the winding currents to estimate the system states [21]. However, linear observers for AMBs are unable to sense the static biases in rotor displacement [22]. It has been shown in simulation that this problem can be solved through the use of a Kalman filter which estimates the bias as a state of the system [23]. However, the robustness of this approach may not be sufficient for practical AMBs. Another approach to creating a self-sensing AMB involves the injection of a high-frequency carrier signal in order to aid in the estimation of the airgap. One variation of this approach [24] developed a nonlinear parameter estimation technique where the noise from the switching amplifier is used to drive the windings as a carrier signal for the modulation of the rotor displacement. In other cases, linear amplifiers are typically used to add a high-frequency carrier signal, where the carrier signal is superimposed on the suspension voltage at a sufficiently high frequency such that the interference with rotor suspension is insignificant. This technique has been successfully demonstrated on a bearingless IM [25].

The rotating magnetic field and harmonics from the PWM drivers in bearingless motors make the airgap estimation more difficult than in magnetic bearings [26]. Methods to estimate the airgap length without sensors have been investigated for bearingless PMSM and IM [25, 27]. To our knowledge this technology for other bearingless motor types has not been studied. In [25] the carrier signal estimation method is applied to a bearingless induction motor where the carrier signal is superimposed on the motor winding and the estimation is based on the change in mutual inductance with rotor position, and in [26] the carrier signal is input to the system through four search coils and the middle-point voltages of these coils are used for the airgap estimation. A similar parameter estimation approach with a carrier signal injected into the motor windings has been developed for a bearingless PMSM [27]. A different approach was used in [28], where a model reference adaptive observer was used for the estimation of the rotor displacement, which has demonstrated good performance without needing to inject a high-frequency signal.

The development of self-sensing bearingless motors is a key technology to enable the wider adoption of bearingless motors. Reducing system costs and size while also improving robustness by enabling the sensorless operation of frictionless motors will allow these machines to be used in a variety of applications. Self-sensing bearingless hystersis-type motors, to our knowledge, have not been studied, but the high-strength rotor coupled with frictionless and sensorless operation would make these machines extremely relevant for high-speed operation in-vacuum or in harsh environments. Therefore, the objective of this thesis project is to develop a method for airgap estimation to enable self-sensing operation of a hysteresis-type motor.

Chapter 3

Operating Principle

This chapter details the operating principle of the hysteresis-type SSBM. First, a 1-DOF example magnetic levitation system will be analyzed, then the same principles will be applied to a bearingless hysteresis motor, followed by an explanation of the airgap estimation method.

3.1 1-DOF magnetic levitation

For an airgap with a length g, permeability in the airgap μ_0, and gap surface area A, the magnetic reluctance of the gap is given as

$$\mathcal{R} = \frac{g}{\mu_0 A}. \tag{3.1}$$

For a coil with N turns and a current of i, the total flux through the coil is

$$\Phi = \frac{Ni}{\mathcal{R}_{total}}, \tag{3.2}$$

where $\mathcal{R}_{total}$ is the total equivalent reluctance of the system.

An E-core magnetic levitation system shown in Figure 3.1 can then be modeled according to the equivalent magnetic circuit shown in Figure 3.2, where $\mathcal{R}_{side}$ is the reluctance of each of the side airgaps with surface area A, and $\mathcal{R}_{center}$ is the reluctance of the central airgap. It is assumed that the permeability in the core is much larger than the permeability in the airgap, so only the reluctance of the airgap is considered in this model.

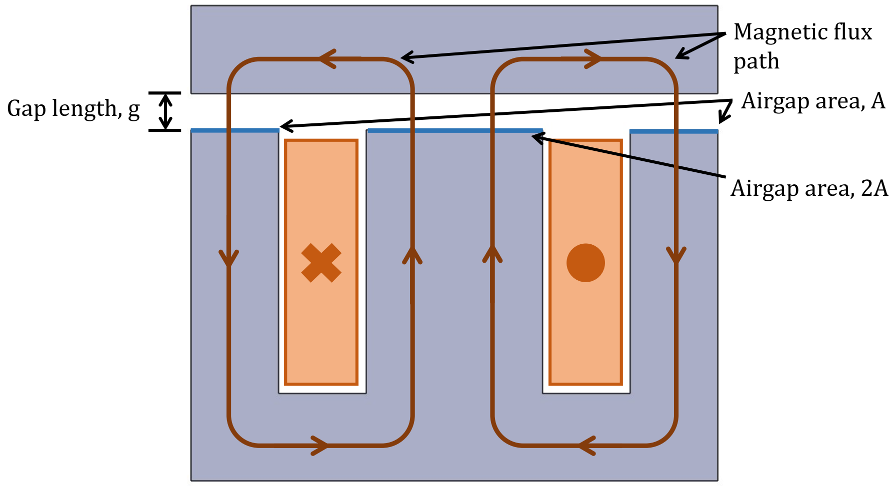

Figure 3.1: 1-DOF example maglev system flux path.

The inductance of the coil is $L = \frac{\lambda}{i}$, where i is the current through the coil, and the flux linkage λ is calculated by $\lambda = N\Phi$. With $L = \frac{N^2}{\mathcal{R}_{eq}}$, the voltage across the coil for the E-core can then be written as

$$v = \frac{N^2}{\mathcal{R}_{eq}} \frac{\mathrm{d}i}{\mathrm{d}t} + Ri, \tag{3.3}$$

where R is the resistance of the coil and $\mathcal{R}_{eq}$ is the equivalent reluctance for the magnetic circuit shown in Figure 3.2.

The inductance of the coil L is directly related to the length of the airgap g. If the current is considered the input to the system, then the output voltage of the coil can be used to estimate the airgap length. In this system, a high frequency carrier signal is injected into the current input to the coil, which effectively amplifies the voltage's sensitivity to airgap length. When the coil's voltage is read as the system output, the signal is demodulated against the high frequency carrier signal, isolating the amplified response dependent on airgap length.

This process was tested on the system shown in Figure 3.3, where the airgap length was varied using plastic shims of various thickness. The coil is connected in series with a power resistor for current sensing, and the current input is generated by a current-controlled amplifier with a gain of $\frac{1\text{A}}{1\text{V}}$. A cRIO-9048 provides the voltage

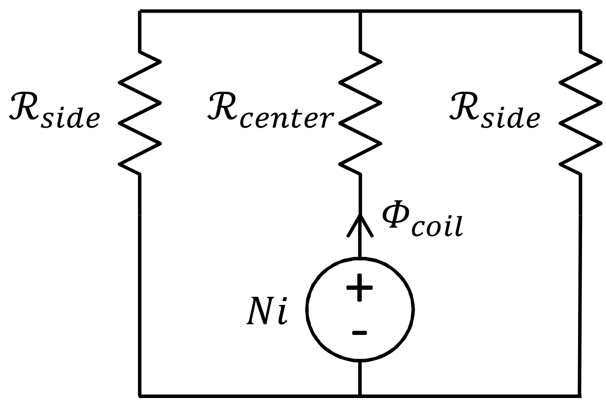

Figure 3.2: Equivalent magnetic circuit for E-core system.

Table 3.1: 1-DOF E-core system parameters

Number of turns, N	120 turns
Airgap cross-sectional area, A	0.74 in^2
Gap length, g	varied from 0 to 0.120 in
Resistance, R	3.1 Ω

input to the board. Dimensions and relevant electrical characteristics of the system are given in Table 3.1. A current with a frequency of 60 Hz and amplitude 0.4 A was added to a high-frequency carrier signal at 2000 Hz and amplitude of 0.1 A to mimic the superposition of the carrier signals in a full motor system. The results of the demodulated voltage signal at 2000 Hz at different airgap lengths are shown in Figure 3.4. There is a clear variation of voltage with respect to the airgap length, as is expected from the governing equations. For the range of airgap lengths tested, the relationship between voltage and airgap length is largely linear. The airgap length was also manually varied to view the transient response of the estimator. The output of the demodulation process for this manual motion is shown in Figure 3.5. These results show the feasibility of the proposed approach for airgap estimation.

Having established the basic self-sensing principle, this concept is then expanded and applied to the full hysteresis motor system.

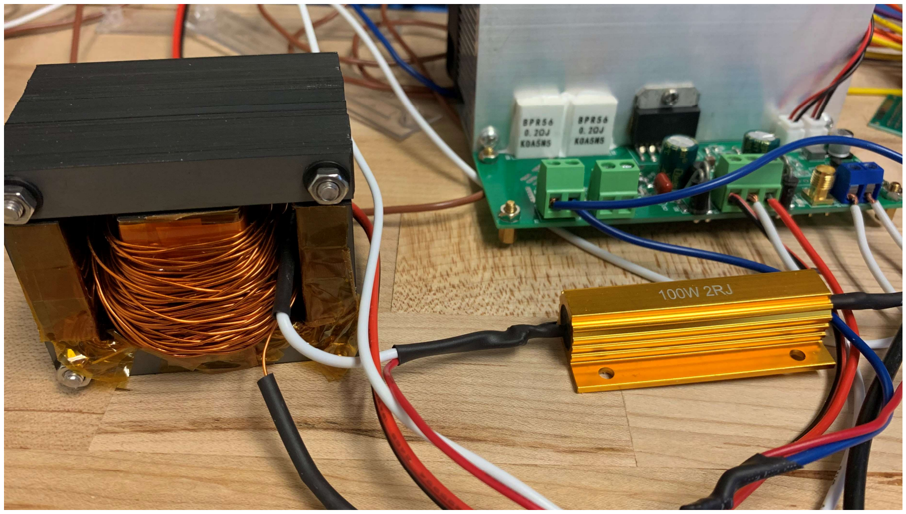

Figure 3.3: 1-DOF example maglev system photo.

3.2 Bearingless operation of a hysteresis motor

Bearingless motors use a single stator assembly to produce both torque and magnetic suspension forces on the rotor. This is accomplished by the superposition of two magnetic fields. The $P\pm2$ principle first proposed in 1974 by Hermann [29] suggests having one magnetic field of P poles and the other of $P\pm2$. Chiba et al. in their book [30] detailed the concept of bearingless motors further. In this design, a two-pole magnetic field is used for the suspension force generation, and a rotating four-pole magnetic field generates the torque. These magnetic fields are generated using a combined winding scheme, requiring 12 independently controlled stator coils.

3.2.1 Torque generation

Our proposed motor uses a hysteresis motor for torque generation. The rotor is a disc of solid D2 tool steel, which is a magnetically semihard material with high permeability for levitation and sufficient magnetic hysteresis to produce a torque in this configuration.

Hysteresis motors operate through the interaction of the stator magnetic field and the hysteresis effect of the rotor material. The magnetic field generated by the stator magnetizes the steel rotor, but as the stator field rotates, the hysteresis effect

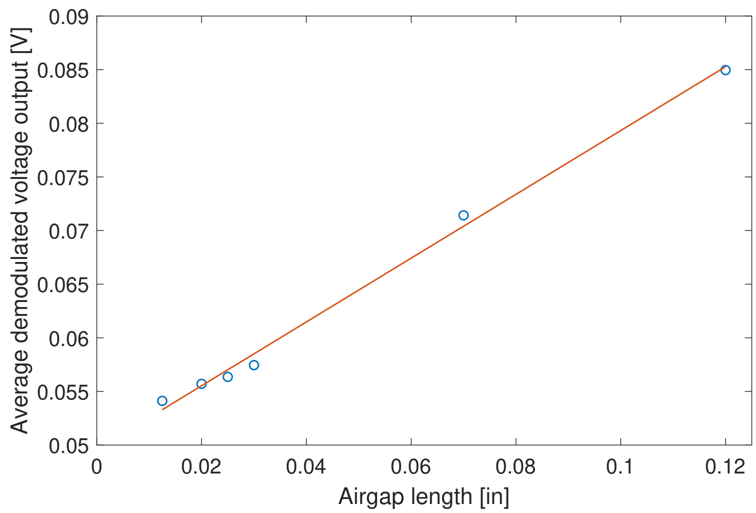

Figure 3.4: 1-DOF example maglev system sampled airgap length demodulation results.

in the rotor causes the induced magnetic field in the rotor to lag behind the field excited by the stator. This phase angle between stator field and rotor magnetization produces a torque [31]. Figure 3.6 illustrates this operating principle, where the torque produced by the motor is related to both the magnitude of the magnetic field and the angle between the stator field and rotor field.

Eddy currents also contribute to torque generation in hysteresis motors, but only before the motor reaches synchronous speed. Due to the difference in speed between the rotor and stator field, eddy currents are generated in the conductive rotor material. The portion of the currents in the axial direction interact with the magnetic field to produce a torque in addition to the hysteresis torque [32]. When the stator and rotor fields reach the same speed, eddy currents are no longer generated, and the motor operates solely on the hysteresis torque production principle.

3.2.2 Suspension force generation

In addition to the four-pole rotating magnetic field, a two-pole magnetic field is added to produce suspension forces. When the two-pole field is oriented as shown in Figure 3.7, the magnetic flux density in the air gap at $\theta = 0°$ becomes smaller

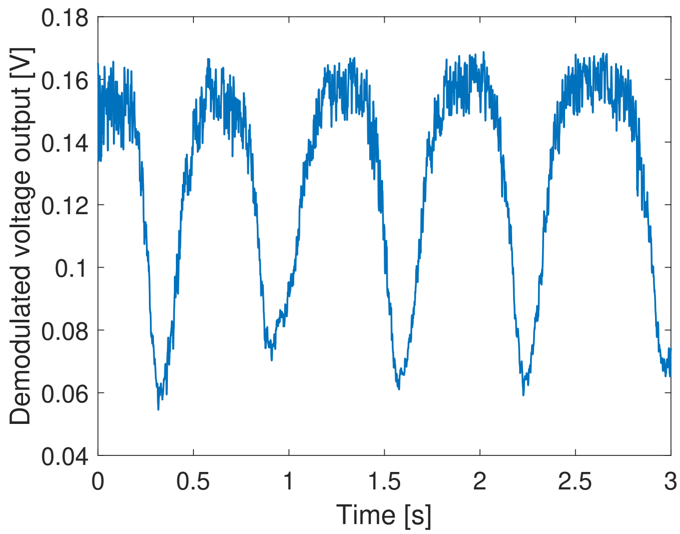

Figure 3.5: 1-DOF example maglev system manual motion demodulation results.

than that of the airgap at $\theta = 180°$. This unbalance in air-gap fluxes generates a force on the rotor in the positive x direction, and serves as the foundation for the reluctance-based suspension force generation for the SSBM.

When only the four-pole magnetic field is present, as in Figure 3.8, any eccentricity of the rotor causes the generation of a radial force in the direction of the narrowest portion of the airgap, where the flux density is greatest. The suspension force is necessary to stabilize the system, as the four-pole motor field creates an inherently unstable system.

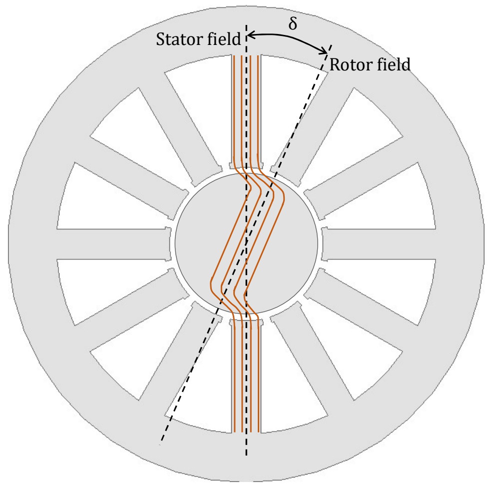

Figure 3.6: Diagram illustrating torque generation principle in a hysteresis motor. Rotor field is displaced by angle δ from the stator field.

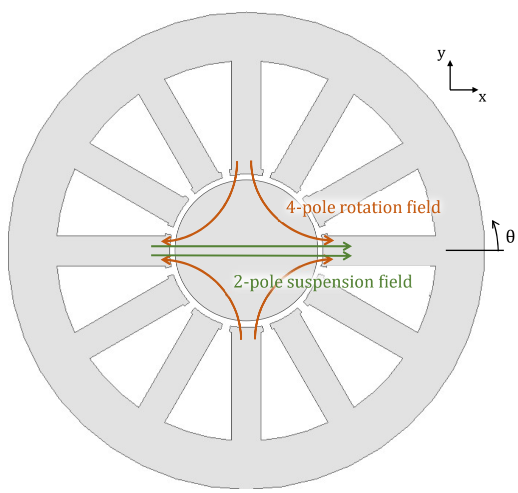

Figure 3.7: Diagram illustrating suspension force generation. In this configuration, the direction of the suspension field causes higher magnetic flux density in the airgap at $\theta = 0\,\mathrm{deg}$, and lower flux density at $\theta = 180\,\mathrm{deg}$, causing a force to be generated in the positive x-direction.

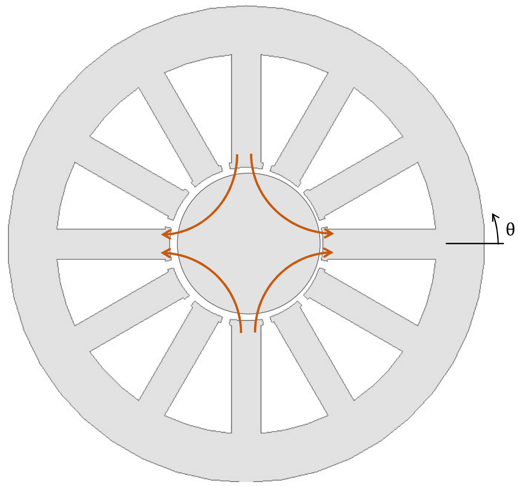

Figure 3.8: Diagram illustrating unstable force generation. In this configuration, the rotor is displaced in the positive x-direction, meaning there is a higher magnetic flux density in the airgap at $\theta = 0\,\text{deg}$ than at $\theta = 180\,\text{deg}$, causing a force to be generated in the positive x-direction, increasing the eccentricity of the rotor.

3.3 Bearingless motor system model

This section presents an analytical model for the suspension and airgap estimation for the bearingless motor. The derivation of the inductance matrix is based on the analysis by Chiba et al in [30], but is modified to match the combined winding scheme utilized in this design. The derivation is also expanded to give an estimation of airgap length based on the stator coil voltages. It is assumed for the purposes of this derivation that the displacement of the rotor is small.

First the winding structure is defined, followed by a derivation of the MMF in the airgap. The next section derives the distribution of magnetic flux. Equations are given for the radial forces generated on the rotor, followed by the stator induction matrix. The induction matrix is used to define the flux linkage in each coil, which is then used to calculate the voltage in each coil. Finally the coil voltages are used to give an estimate of airgap length.

3.3.1 Winding diagram

Bearingless motors typically employ either a combined or distributed winding scheme. Distributed windings use separate coils to carry the suspension and rotation currents, meaning that the proportion of the slot used for suspension force generation is fixed, and must be sufficient to generate the maximum force required by the system at any time. When using a combined winding scheme, the same coils are used to carry both suspension and rotation currents, meaning that the windings can dynamically adjust the portion of the wire's allowable current density used to generate suspension force or torque [33]. However, this design complicates the electronics required to drive the motor, as standard three-phase winding configurations cannot be used without modification.

Our design utilizes a combined winding scheme, where 12 stator coils are each independently controlled to generate a four-pole magnetic field for rotation superimposed on a two-pole magnetic field for suspension. The winding pattern is shown in Figure 3.9.

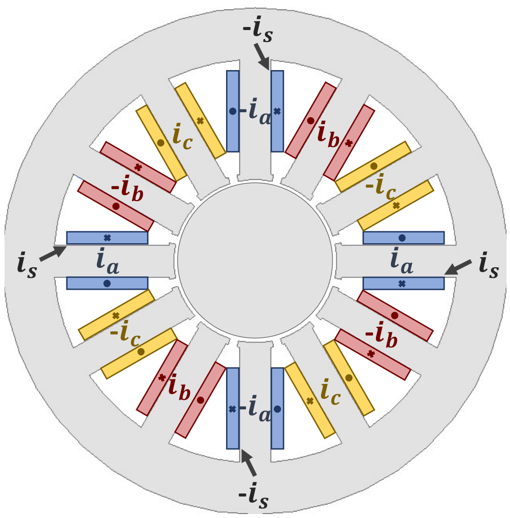

(a) 4-pole rotation currents

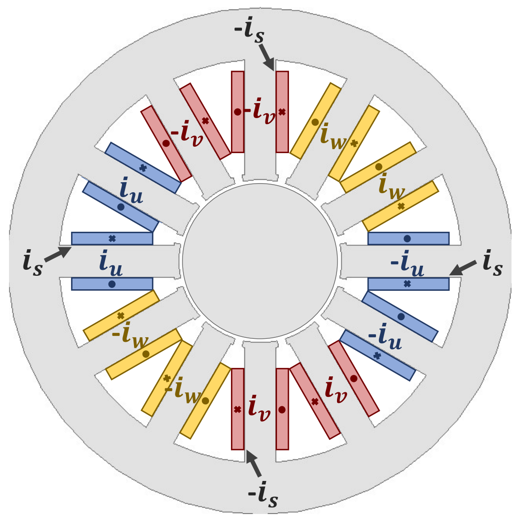

(b) 2-pole suspension currents

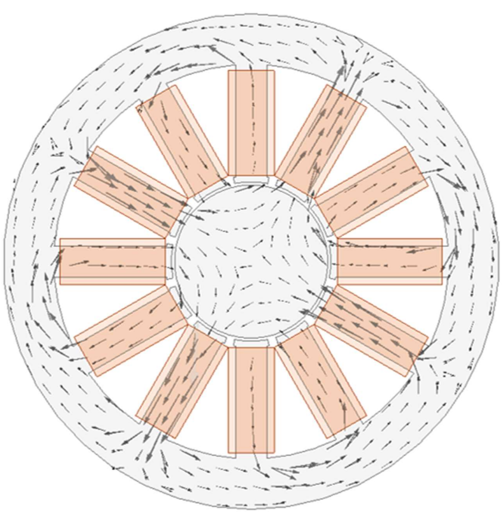

(c) 4-pole rotation magnetic field

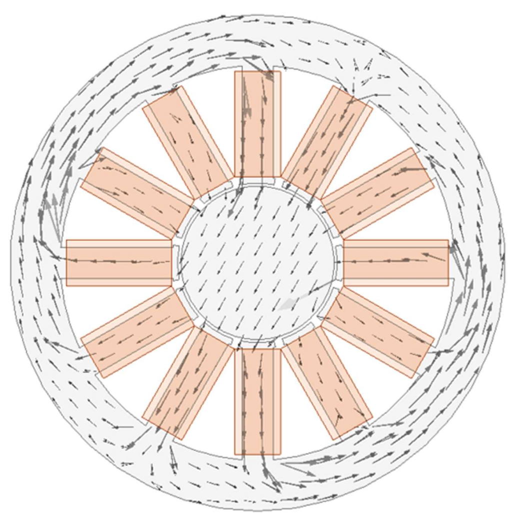

(d) 2-pole suspension magnetic field

Figure 3.9: Winding diagram and with corresponding magnetic fields.

3.3.2 Airgap length and MMF distribution

The air-gap estimation studied in this work is based on the variation of coil inductance with air-gap length, as introduced in the 1-DOF example system. The x- and y- axes are used to define the two radial degrees of freedom of the rotor, so the nominal airgap length at any angle θ around the stator can be calculated as in (3.4), pictured in Figure 3.10. Assuming the rotor's radial displacement is small and ignoring higher order terms of the Taylor series expansion, the inverse of the airgap can be approximated as (3.5). Here g_0 is the nominal airgap length, x and y are the coordinates of the center of the rotor, and θ is the angular position where the airgap length is being calculated.

$$g = g_0 + x\cos\theta + y\sin\theta, \tag{3.4}$$

$$\frac{1}{g} \approx \frac{1}{g_0}\left(1 + \frac{x}{g_0}\cos\theta + \frac{y}{g_0}\sin\theta\right). \tag{3.5}$$

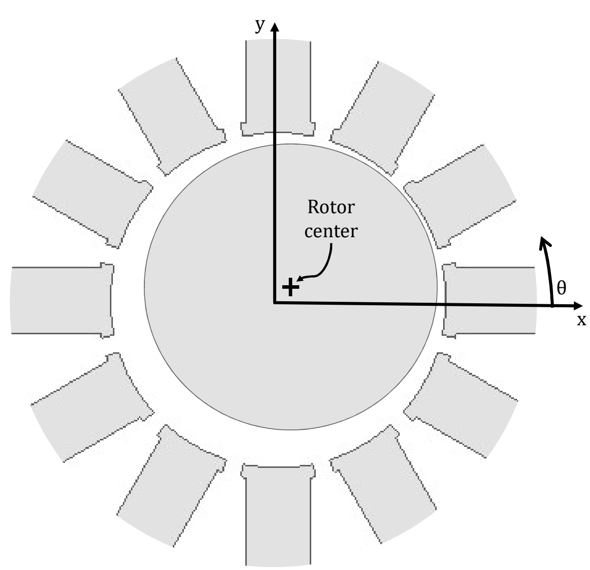

Figure 3.10: Airgap length variation due to rotor eccentricity. Airgap length depends on rotor center coordinates x and y along with angular position θ.

Using this formulation of the airgap length, the permeance at angular position θ is then calculated as

$$P_0(x, y, \theta) = \frac{\mu_0 r l}{g_0} \left(1 + \frac{x}{g_0}\cos\theta + \frac{y}{g_0}\sin\theta\right), \tag{3.6}$$

where r is the rotor radius, μ_0 is the permeability of free space, and l is the motor length.

Assuming equal current and an equal number of turns, N, in each coil, the MMF space distribution A_i with respect to angular position is of the form shown in Figure 3.11. MMF is defined as Ni, so over the angular range of the tooth corresponding to a particular coil, the magnitude of the MMF for coil i is $A_i = Ni_i$. This distribution is then shifted down to account for the magnetic potential of the rotor, which will be discussed in more detail in the following section. Each of the 12 windings has an MMF distribution of the same form, where the positive portion of the distribution occurs over the angle corresponding to that winding's position.

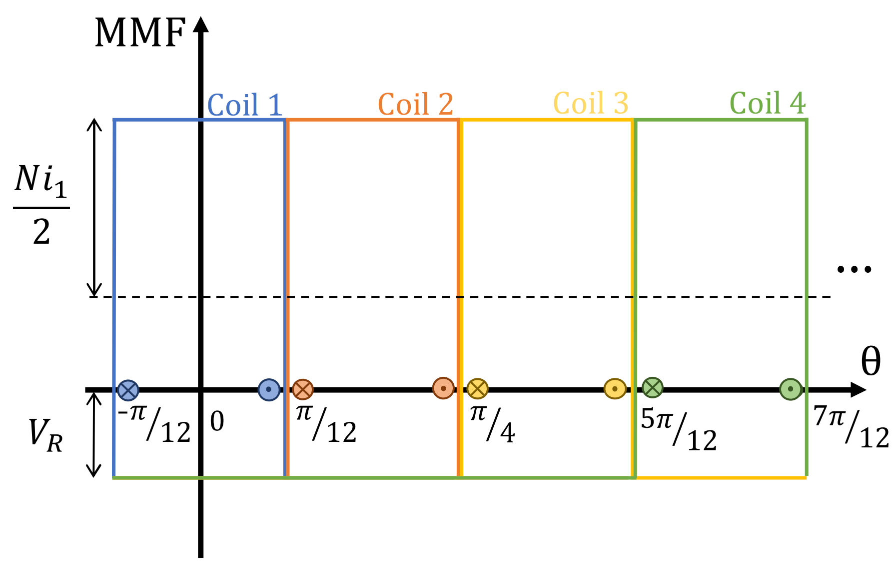

Figure 3.11: MMF space distribution for coils 1 to 4 assuming equal current in all coils. Distribution is shifted up to account for rotor potential, V_r.

3.3.3 Magnetic flux distribution and rotor potential

Next, the flux distribution in the airgap is derived. It is important to consider the non-zero magnetic potential of the rotor due to the asymmetrical distribution of flux caused by rotor displacement. According to Gauss' law, the integral of the magnetic flux through a closed surface surrounding the rotor must be zero, as

$$\int_0^{2\pi} \phi\left(\theta\right) \mathrm{d}\theta = 0. \tag{3.7}$$

With the previously defined winding MMF distribution A_i, the airgap permeance as a function of angular position $P_0\left(x, y, \theta\right)$ and the necessary inclusion of the rotor's magnetic potential V_r, the flux in the airgap as a function of angle θ can be written as

$$\phi_i(\theta) = P_0(x, y, \theta)(A_i + V_r). \tag{3.8}$$

To calculate the rotor magnetic potential V_r, equations (3.7) and (3.8) are combined. This gives an expression for rotor potential due to the excitation of one coil i of the form

$$V_{r,i} = -\frac{\int_0^{2\pi} P_0(x, y, \theta) A_i \mathrm{d}\theta}{\int_0^{2\pi} P_0(x, y, \theta) \mathrm{d}\theta}. \tag{3.9}$$

3.3.4 Inductance matrix and coil voltage

The self and mutual inductances for each coil can be calculated as

$$L_{i,i} = \int_0^{2\pi} A_i \phi_i \mathrm{d}\theta, \tag{3.10}$$

$$M_{i,j} = \int_0^{2\pi} A_i \phi_j \mathrm{d}\theta. \tag{3.11}$$

These form a 12×12 matrix $L(x, y, \theta)$, which gives the equation for flux linkage of each coil in matrix form as

$$\begin{bmatrix} \lambda_1 \\ \lambda_2 \\ \lambda_3 \\ \vdots \\ \lambda_{11} \\ \lambda_{12} \end{bmatrix} = \begin{bmatrix} L_{1,1} & M_{1,2} & M_{1,3} & \dots & M_{1,11} & M_{1,12} \\ M_{2,1} & L_{2,2} & M_{2,3} & \dots & M_{2,11} & M_{2,12} \\ M_{3,1} & M_{3,2} & L_{3,3} & \dots & M_{3,11} & M_{3,12} \\ \vdots & \vdots & \vdots & \ddots & \vdots & \vdots \\ M_{11,1} & M_{11,2} & M_{11,3} & \dots & L_{11,11} & M_{11,12} \\ M_{12,1} & M_{12,2} & M_{12,3} & \dots & M_{12,11} & L_{12,12} \end{bmatrix} \begin{bmatrix} i_1 \\ i_2 \\ i_3 \\ \vdots \\ i_{11} \\ i_{12} \end{bmatrix}. \tag{3.12}$$

3.3.5 Radial force

The radial force acting on the rotor is calculated from the inductance matrix by first writing the magnetic coenergy W_m as

$$W_m = \frac{1}{2}[i]^t[L(x, y, \theta)][i], \tag{3.13}$$

where $[i]$ is a vector of the currents in the stator windings.

Assuming a magnetically linear system, the force is then calculated by taking the partial derivative of the stored magnetic energy with respect to both x and y, written as

$$\begin{bmatrix} F_x \\ F_y \end{bmatrix} = \begin{bmatrix} \frac{\partial W_m}{\partial x} \\ \frac{\partial W_m}{\partial y} \end{bmatrix}. \tag{3.14}$$

3.3.6 Airgap length estimation

The calculated inductance values form a 12×12 matrix $L(x, y, \theta)$, which can then be used to find the voltage in the coils as

$$\begin{bmatrix} v_1 \\ v_2 \\ \vdots \\ v_{12} \end{bmatrix} = \begin{bmatrix} R_1 & 0 & \dots & 0 \\ 0 & R_2 & \dots & 0 \\ \vdots & \vdots & \ddots & \vdots \\ 0 & 0 & \dots & R_{12} \end{bmatrix} \begin{bmatrix} i_1 \\ i_2 \\ \vdots \\ i_{11} \\ i_{12} \end{bmatrix} + \begin{bmatrix} L_{1,1} & M_{1,2} & \dots & M_{1,12} \\ M_{2,1} & L_{2,2} & \dots & M_{2,12} \\ \vdots & \vdots & \ddots & \vdots \\ M_{12,1} & M_{12,2} & \dots & L_{12,12} \end{bmatrix} \begin{bmatrix} \frac{di_1}{\mathrm{d}t} \\ \frac{di_2}{\mathrm{d}t} \\ \vdots \\ \frac{di_{12}}{\mathrm{d}t} \end{bmatrix} + \begin{bmatrix} E_{b,1} \\ E_{b,2} \\ \vdots \\ E_{b,12} \end{bmatrix} \tag{3.15}$$

Here v and i are vectors of the 12 coil voltages and currents, respectively, and $\mathbf{R}_{12\times12}$ is the resistance matrix of the winding coils. E_b represents the back-emf, which is small in a hysteresis motor and thus this term is negligible.

In this way, the voltage in each coil is dependent on the rotor's position, and an estimated air gap signal can be achieved by demodulation of the stator voltage signals.

To amplify the effect of changing air-gap length on coil voltage, high frequency current signals are injected into the four coils aligned with the x and y-axes, i_1, i_4, i_7, and i_{10}. The high frequency component of the voltage signals in these coils is dominated by the inductance of the coil, so when these signals are demodulated against the injected high frequency carrier signal, the result is closely related to the inductance of the coils and thus the length of the airgap.

More details on the implementation of the airgap estimation will be provided in Chapter 5.

3.4 Analytical modeling results

Having developed the analytical models for the motor, simulations for the system under both voltage and current control were conducted using the analytical model to validate the estimation approach. This section summarizes the results from those simulations. The complete MATLAB code for the analytical model can be found in Appendix A.

3.4.1 Model summary

The analytical model was based on the equations derived in the previous section. For this simulation, one adjustment was made to the nominal gap length g_0 in equation (3.4). To adjust for the effect of slot leakage, Carter's coefficient K_c was included in the gap length such that the equation for permeance became

$$P_0(\theta) = \frac{\mu_0 r h}{K_c g_0}\left(1 + \frac{x}{K_c g_0}\cos(\theta) + \frac{y}{K_c g_0}\sin(\theta)\right). \tag{3.16}$$

Carter's coefficient is written as

$$K_c = \frac{\tau_t}{\tau_t - \gamma \cdot g_0}, \tag{3.17}$$

where τ_t is the slot-pitch, g_0 is the nominal airgap length, and γ is calculated as

$$\gamma = \frac{4}{\pi}\left(\frac{b_0}{2g_0}\arctan\frac{b_0}{2g_0} - \ln\sqrt{1+\left(\frac{b_0}{2g_0}\right)^2}\right), \tag{3.18}$$

where b_0 is the slot-opening width. More details on the use of Carter's coefficient are presented in [34].

3.4.2 Simulation results under current control

Appendix A.2.2 presents the full MATLAB script for the simulation of the system under current control. Figure 3.12 shows the estimation result from the analytical model. There is a clear nonlinear relationship between rotor displacement and the high-frequency component of the stator voltage. Demodulating the voltage signal isolates the high frequency component of the signal and gives a good basis for the airgap estimation.

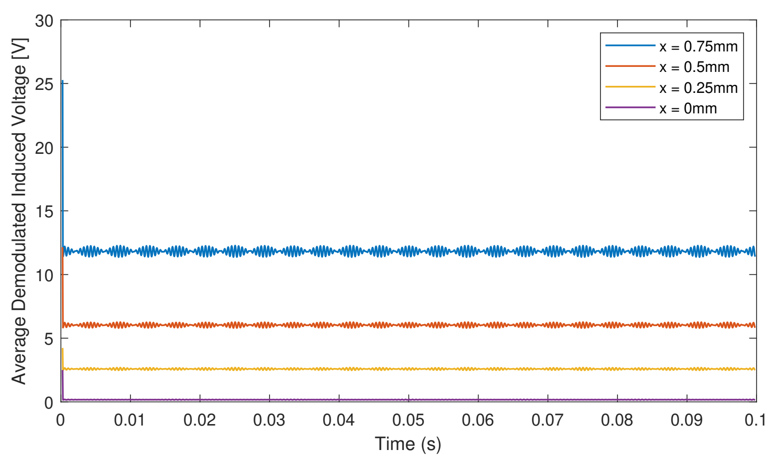

Figure 3.12: Results from analytical model for the system under current control.

3.4.3 Simulation results under voltage control

Appendix A.2.1 contains the full MATLAB script for the simulation of the system under voltage control. Figure 3.13 shows the estimation result from the analytical model. Unlike the result from the current control simulation, this result does not show a clear correlation between rotor displacement and estimation output. The inductance of the stator windings impedes the high-frequency current response, so the carrier signal is unable to amplify the winding response enough to make the estimation effective.

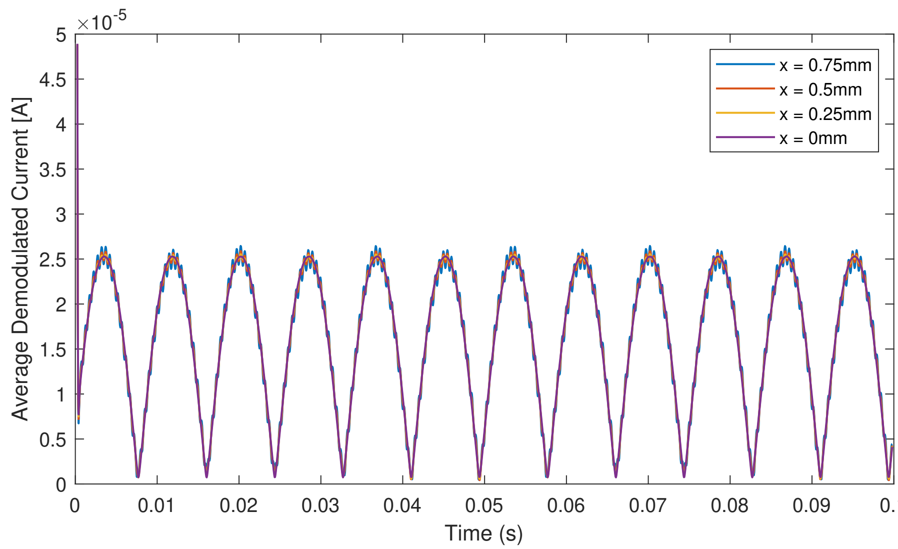

Figure 3.13: Results from analytical model for the system under voltage control.

3.5 Summary

The proposed system is a hysteresis-type bearingless motor where the airgap estimation is enabled through the use of a high-frequency carrier signal injected into the stator windings. In this chapter an analytical model for a bearingless motor was developed to validate the proposed approach. First, the sensing method was implemented for a 1-DOF E-core system, which demonstrated a linear relationship between demodulated coil voltage and airgap length within the tested range. The same sensing principle was then expanded to a bearingless motor and a complete analytical model was developed. Simulation results show that under current control the proposed technique gives a clear variation in estimation result for different rotor displacements. The simulation was modified such that voltages were input to the stator windings and current was used for the estimation process, but did not give a good estimate for airgap length. The amplitude of the carrier signal needs to be much larger to provide a good estimate of rotor position. Having established the feasibility of the estimation method, the following chapter will describe the hardware developed for experimental evaluation of the approach.

Chapter 4

Hardware Implementation

We have designed and built a SSBM prototype to test the proposed estimation approach. This chapter describes the design and hardware implementation details of the SSBM.

4.1 System overview

The SSBM prototype consists of a magnetically levitated disc-shaped rotor that rotates about the vertical axis and a stator assembly which provides both torque and suspension forces. Figures 4.1 and 4.2 show the CAD design of the SSBM. To enable simple airgap estimation, a hysteresis-type bearingless motor is selected, since it allows the use of a cylindrical rotor made of a highly permeable material. The whole assembly is 8 in tall from the top of the base plate and is mounted on an 8 in $\times$ 8 in optical breadboard. The rotor is attached to a vertical shaft that also supports a low-carbon steel disc which provides a target for four inductive sensors to measure the horizontal displacement of the rotor. The vertical shaft is constrained at one point by a tooling ball at its base. The four inductive sensors are mounted on a resin stereolithography (SLA) printed stand, which is bolted to the optical breadboard. The stator has 12 slots and 12 independently controlled windings, and is mounted to an aluminum plate at the top of the assembly.

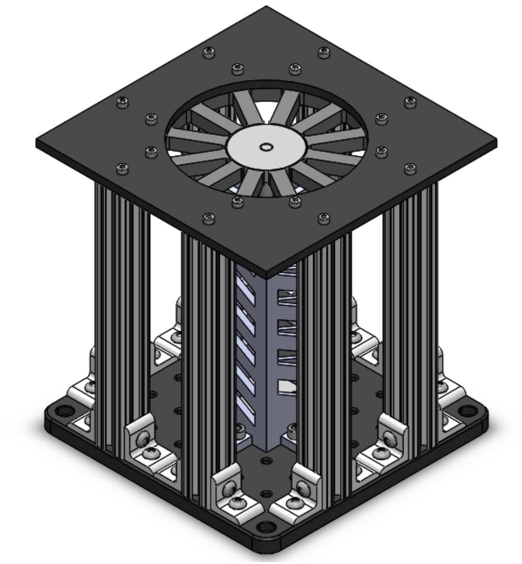

Figure 4.1: CAD design of SSBM.

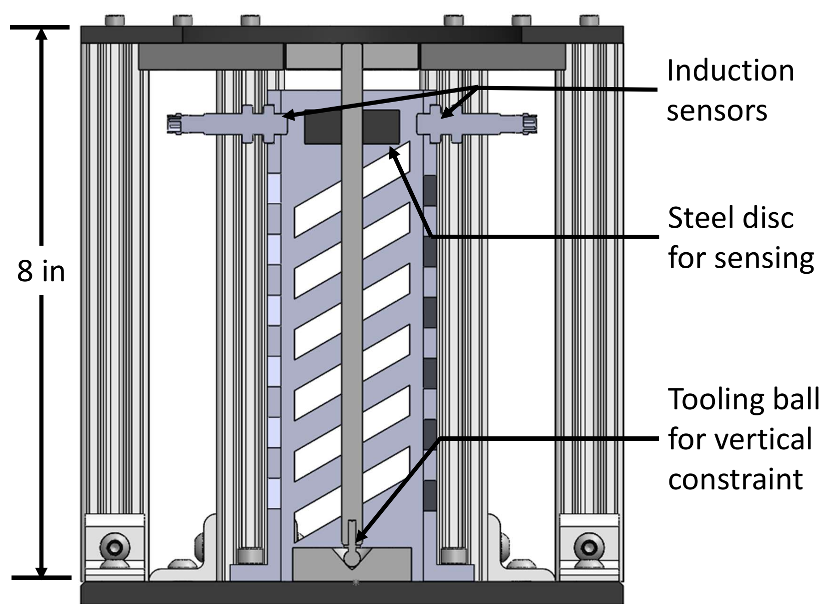

Figure 4.2: Section view of CAD design of SSBM.

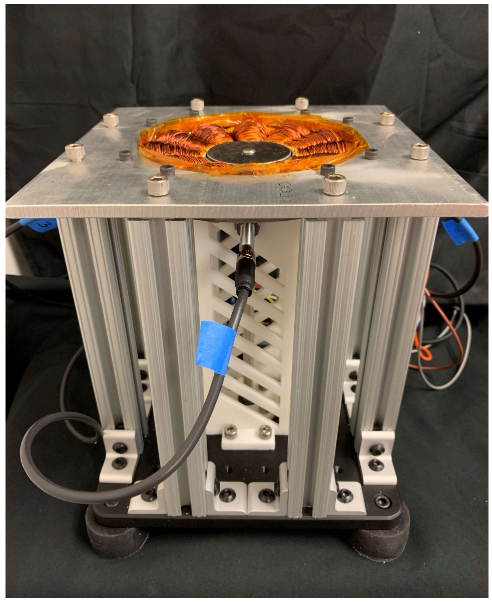

Figure 4.3: Photograph of SSBM assembly.

4.2 Rotor

The rotor is a 10 mm thick disc with a 49.5 mm diameter machined by water-jet cutting from unhardened D2 tool steel. D2 tool steel has previously been used as a rotor material in hysteresis motors [15]. D2 steel has sufficient magnetic hysteresis properties and is easily accessible, making it a good rotor material for this project. D2 tool steel has proved adequate for testing the self-sensing ability of the SSBM design, but to improve the torque performance of the motor, the D2 steel would either have to be hardened to improve the hysteresis properties or a different material, for example a chrome-cobalt alloy, could be chosen [15].

This design constrains the rotor in z, θ_x, and θ_y DOFs, and allows it to move in x, y, and θ_z DOFs. The rotor is constrained in the vertical direction by a tooling ball of diameter 0.25 in at the bottom of the rotor shaft, as shown in Figure 4.4. A cone shaped indentation in the base block of aluminum constrains the tooling ball at the end of the shaft. The rotor's radial position is actively controlled by the 2-pole magnetic field generated by the stator coils.

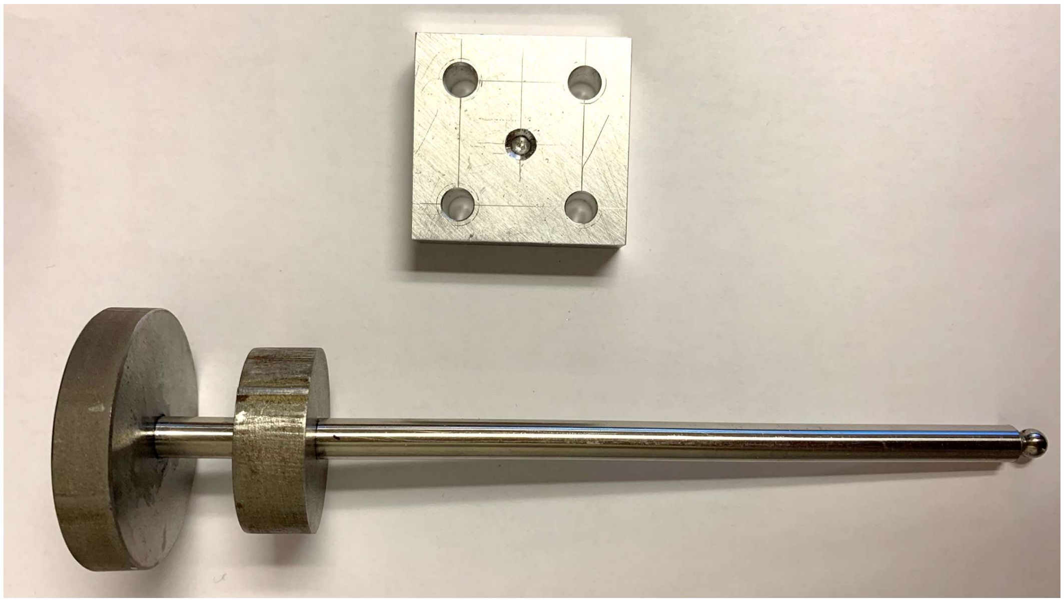

Figure 4.4: Photograph of assembled shaft with tooling ball constraint.

4.3 Stator

The stator core is comprised of 20 layers of M19 steel laminations which are each 0.5 mm thick for a total stator thickness of 10 mm, as shown in Figure 4.5. The laminations are held in place by 8 M4 bolts that pass through the through-holes in the laminations and the top plate, securing the stator to the frame of the assembly. The stator laminations were laser cut to have an outer diameter of 160 mm and an inner diameter of 51.5 mm to allow for a 1 mm airgap length between the rotor and stator.

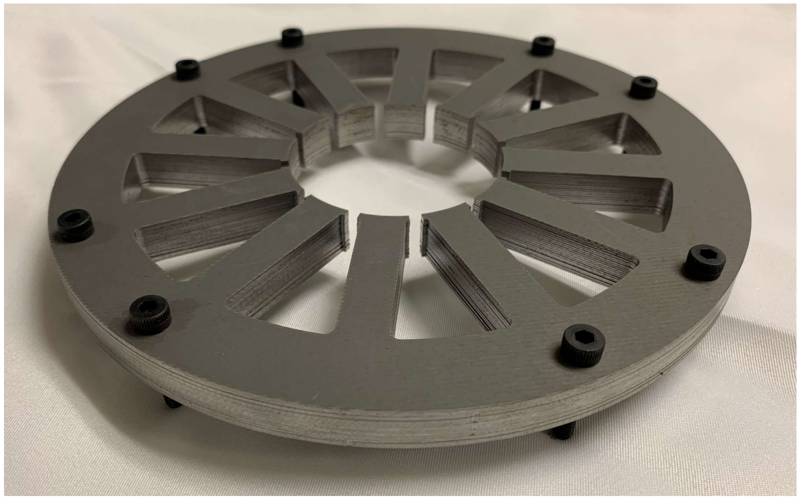

Figure 4.5: Photograph of stator laminations.

The stator in the SSBM prototype uses a combined winding scheme [33], superimposing the suspension and rotation currents in the same windings. As such, each of the 12 stator windings must be independently controlled and are wound separately with one coil around each stator tooth. The windings each have 200 turns and are made of epoxy-bondable magnetic wire from MWS of AWG22. The stator core is insulated from the windings by Nomex 410 insulation paper and Kapton tape. Figure 4.6 shows the stator with the finished windings.

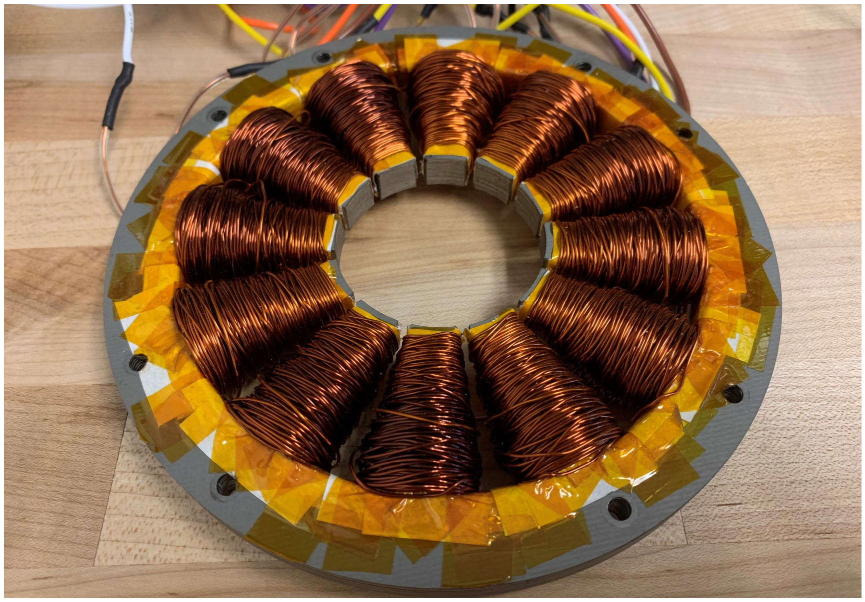

Figure 4.6: Photograph of fully insulated stator with 12 copper windings.

4.4 Inductive sensors

Four inductive sensors, Contrinex DW-AS-509, are mounted around the rotor shaft at 6.75 in from the base, or 1.2 in from the top of the rotor. The sensors are mounted using nuts adhered in the hexagonal spaces designed on an SLA printed sensor stand. A low carbon steel disc with a diameter of 1.4 in is attached to the shaft, providing a target for the sensors. In this way the sensors measure the rotor's radial position, providing a "ground truth" signal for the air gap estimation problem. The shaft assembly with the sensing disc is shown in Figure 4.4, and the sensors mounted on the sensor stand are shown in Figure 4.7.

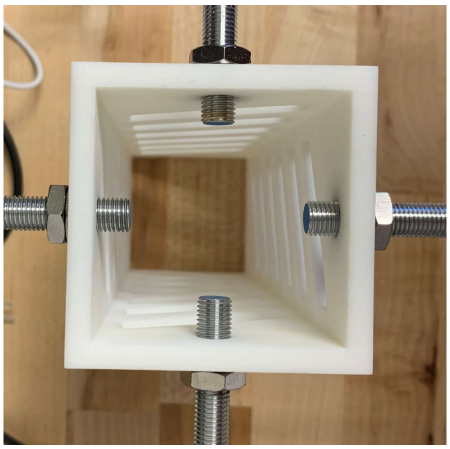

(a) Top view

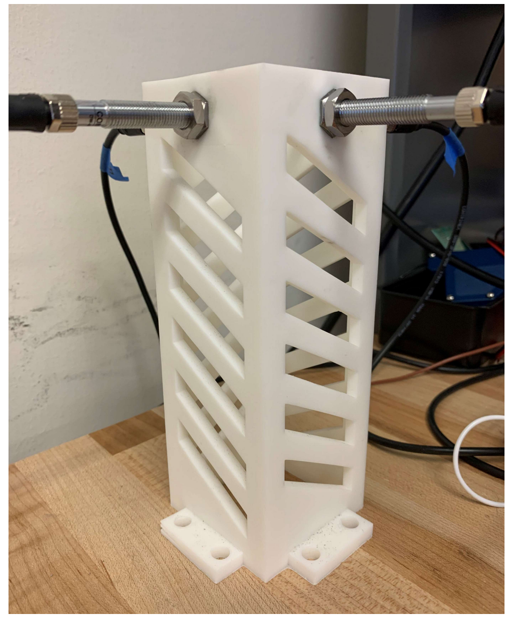

(b) Side view

Figure 4.7: Photographs of inductive sensors and SLA printed stand.

4.5 Power amplifiers

The 12 stator windings are controlled by a NI compactRIO 9048 whose signals are amplified by an array of 12 linear power amplifier PCBs, OPA541 by Texas Instruments. Current control for the system has been designed but not implemented, and will be further discussed in Chapter 5. Figure 4.8 shows the 12 linear power amplifiers and the 12 sensing resistors of resistance 2 Ω that enable measurement of the stator currents. The linear power amplifiers are assumed to have a constant gain of 6.

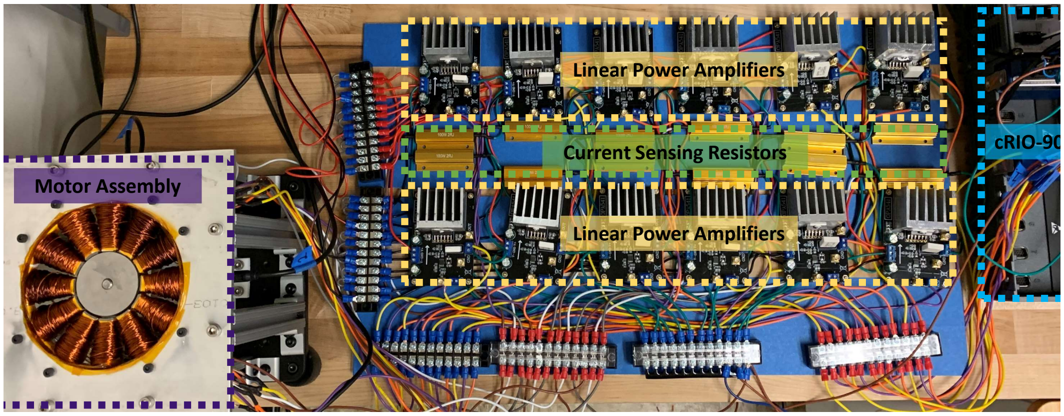

Figure 4.8: Photograph of full setup including power amplifier array with current sensing resistors.

4.6 Summary

This chapter provides an overview of the hardware design of the SSBM. In the following chapter the control and estimation design for this prototype will be described.

Chapter 5

Control and Estimation Design

5.1 Overview

This chapter discusses the control system and the estimation method that enables the self-sensing operation of the motor prototype. First, the suspension control loop will be discussed including the coordinate transformations used to enable field-oriented control. Next the torque command generation will be addressed. The next two sections cover the difference between current and voltage control, and how each is used to implement the magnetic levitation of the rotor. Finally the estimation techniques are discussed. The digital portion of the control loop was implemented in LabVIEW on a cRIO-9048. Figure 5.1 shows the block diagram for the full system under current control.

5.2 Suspension control

The magnetic levitation of the rotor is inherently unstable due to the negative stiffness of the system in the radial DOFs. If the rotor is displaced from the center of the stator bore, the reluctance of the gap in the direction of displacement becomes smaller, making the flux density and reluctance force increase in that direction. This is illustrated in Figure 5.2, where the rotor is displaced in the positive x-direction, which increases the flux density in the gap located at $\theta = 0°$ and decreases the flux density in the gap at $\theta = 180°$. This causes a reluctance force to act on the rotor, pushing it in the positive x-direction, making the system unstable. As such,

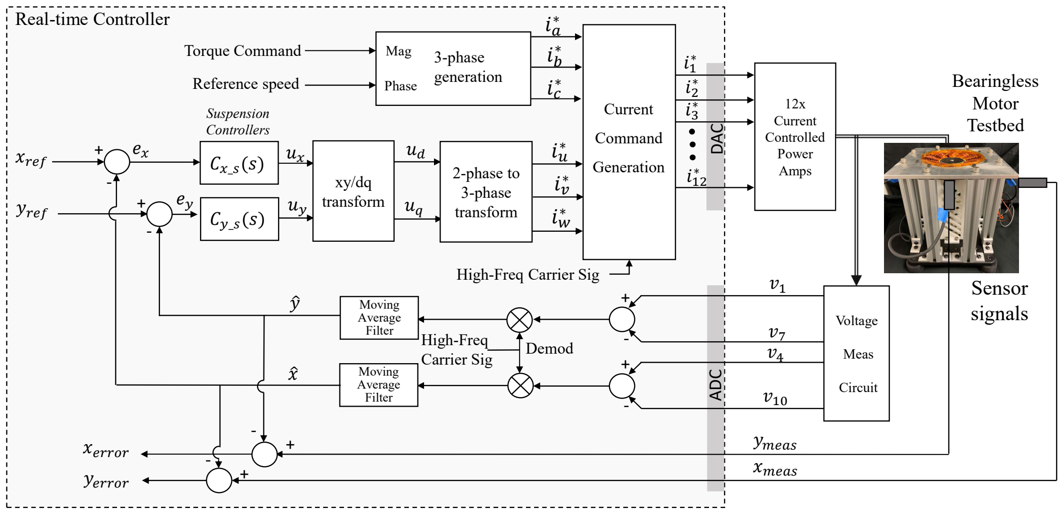

Figure 5.1: Self-sensing bearingless motor control block diagram.

it is necessary to implement closed-loop feedback control loops to enable the stable magnetic levitation of the rotor. Figure 5.3 shows the portion of the block diagram dedicated to suspension control. The error signals, e_x and e_y, correspond to the two radial degrees of freedom and are defined as the difference between the reference and the position reading from the estimation process. These signals are passed through linear controllers to compute the control effort for the x- and y-direction, u_x and u_y. These effort signals are transformed into the rotational d-q coordinate system control efforts u_d and u_q using the Park transformation. More details of the transformations can be found in [35]. The angle for the transformation is determined by the airgap field orientation. This is added to a phase shift $\frac{\pi}{12}$ to align the 2-pole suspension field with the 4-pole rotation field, so the angle for the Park transformation is $2\omega t + \frac{\pi}{12}$. This is written as

$$\begin{bmatrix} u_d \\ u_q \end{bmatrix} = \begin{bmatrix} \cos(2\omega t + \frac{\pi}{12}) & \sin(2\omega t + \frac{\pi}{12}) \\ \sin(2\omega t + \frac{\pi}{12}) & -\cos(2\omega t + \frac{\pi}{12}) \end{bmatrix} \begin{bmatrix} u_x \\ u_y \end{bmatrix}. \tag{5.1}$$

To generate the three-phase current commands required by the windings, u_d

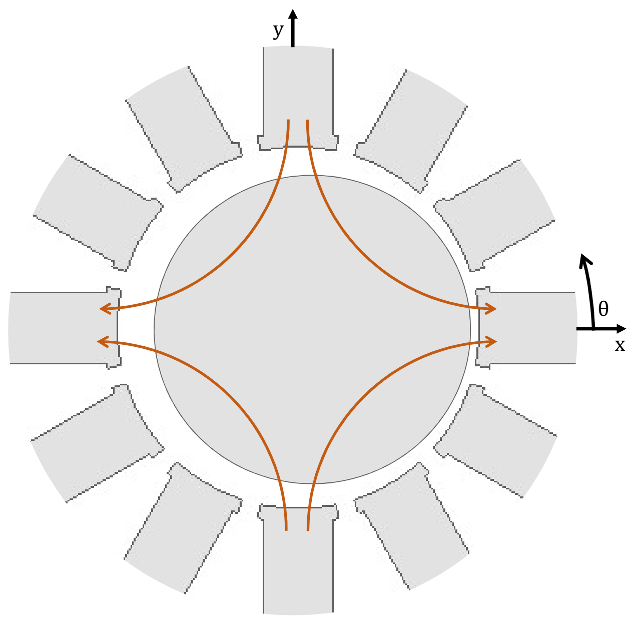

Figure 5.2: When the rotor is displaced from the center, the flux density in the smaller airgap from the 4-pole magnetic field increases, causing a destabilizing reluctance force to act on the rotor.

and u_q are then transformed from 2-phase into 3-phase signals by

$$\begin{bmatrix} i_u \\ i_v \\ i_w \end{bmatrix} = \begin{bmatrix} 1 & 0 \\ -\frac{1}{2} & \frac{\sqrt{3}}{2} \\ -\frac{1}{2} & -\frac{\sqrt{3}}{2} \end{bmatrix} \begin{bmatrix} u_d \\ u_q \end{bmatrix}. \tag{5.2}$$

These transformations are further illustrated in Figure 5.4. The key idea is that the sensing, error calculation, and linear controller are implemented with respect to the x-y axes, but the 3-phase suspension current is generated with respect to the rotational d-q axes of the rotor.

To stabilize the magnetic suspension of the rotor, double lead controllers with an integral term were used, following the form in equation (5.3). The system

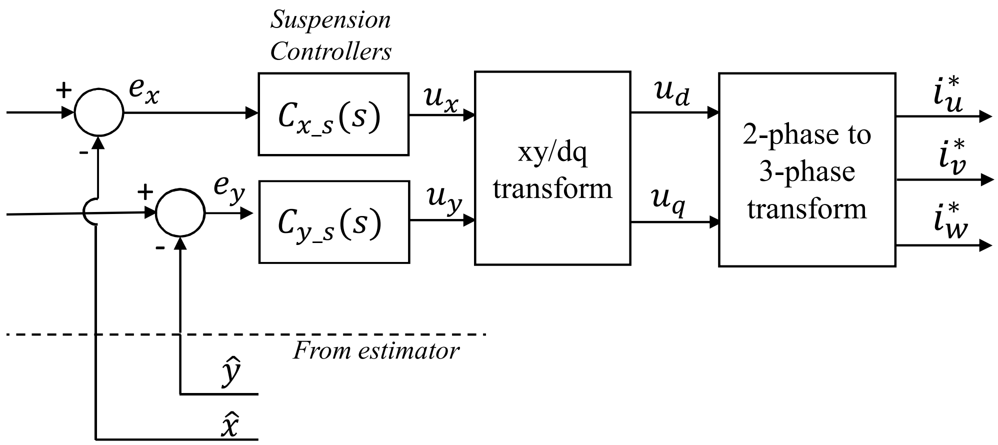

Figure 5.3: Suspension control block diagram

is assumed to be symmetrical, so identical controllers can be used to stabilize the x- and y- degrees of freedom.

$$C_x(s) = C_y(s) = K \left(\frac{\alpha \tau s + 1}{\tau s + 1} \right)^2 \left(1 + \frac{1}{T_i s} \right). \tag{5.3}$$

The coordinate transformation and suspension controller form remain the same for both voltage and current control, but the controller parameters differ due to the change in plant transfer function.

5.3 Torque command generation

Our bearingless motor is operated under open-loop commutation, where the generation of torque current commands is simple. The desired magnitude and rotational speed of the 4-pole field are input and again transformed using the Park and Clarke transformations, writing the input first in d- and q-coordinates and then as 3-phase commands, written as

$$\begin{bmatrix} u_{\tau,d} \\ u_{\tau,q} \end{bmatrix} = \begin{bmatrix} \cos(2\omega t) & \sin(2\omega t) \\ \sin(2\omega t) & -\cos(2\omega t) \end{bmatrix} \begin{bmatrix} \tau_{mag} \\ 0 \end{bmatrix}, \tag{5.4}$$

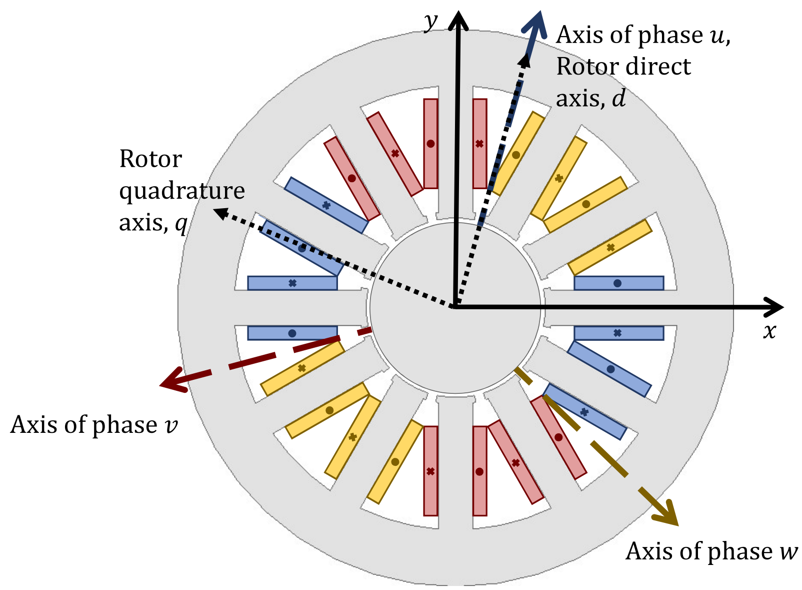

Figure 5.4: Field-oriented control transformation illustration

$$\begin{bmatrix} i_a \\ i_b \\ i_c \end{bmatrix} = \begin{bmatrix} 1 & 0 \\ -\frac{1}{2} & \frac{\sqrt{3}}{2} \\ -\frac{1}{2} & -\frac{\sqrt{3}}{2} \end{bmatrix} \begin{bmatrix} u_{\tau,d} \\ u_{\tau,q} \end{bmatrix}. \tag{5.5}$$

Note that there is no phase shift in the torque current formulation, as the adjustment needed to align the torque and suspension fields was made in the suspension current transformation. As such, the torque current commands i_a, i_b, and i_c are output by the cRIO to the stator windings according to the winding diagram in Figure 3.9.

5.4 Voltage control

For the system under voltage control, the voltage singals output by the cRIO were amplified by linear power amplifiers (OPA541, Texas Instruments) with the gain set to 6. The dynamics of the amplifiers are ignored. This is not the ideal way to drive the motor, as the suspension force is linearly related to the suspension current in the coils. However, it is possible to stabilize the system under voltage control, as the same equations still hold; the only difference in this configuration is the voltage is considered the input and the winding current is taken as the output. The block diagram for voltage control is shown in Figure 5.5. This diagram is similar to that for current control, the key differences being the voltage commands for torque and suspension force, and the current measurements that are read back for the estimation process. These currents are measured using the voltages across the power resistors connected in series to the stator windings.

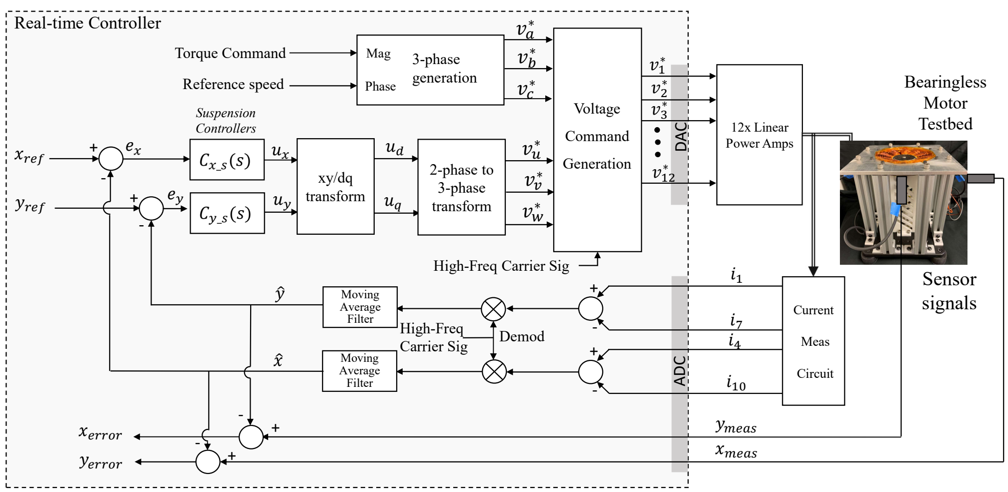

Figure 5.5: Block diagram for system under voltage control

5.4.1 Air-gap estimation

As outlined in the operating principle equations, the air-gap length is related to current by the changing inductance caused by variable rotor position. For the system under voltage control, the input for the estimation function is the winding currents, as in Figure 5.6. The same algorithm is used when the system is under current control, the only difference is the use of winding voltage instead of current as the system output used for estimation.

The currents through coils 1, 4, 7, and 10, which are aligned with the positive and negative x- and y- axes, are input to the cRIO and demodulated against the high-frequency signal according to the diagram shown in Figure 5.6. First the current differential in the coils for each axis is calculated, $i_1 - i_7$ for the x-axis, and $i_4 - i_{10}$ for the y-axis. These signals are then multiplied by both cosine and sine of the carrier frequency, $f_{sens} = 2$ kHz. Next each signal is averaged over a window with N samples, where $N = \frac{F_s}{f_{sens}}$, $F_s = 10$ kHz is the sampling frequency, and f_{sens} is the frequency of the high-frequency carrier signal, in this case 2 kHz. To find the estimated value for the magnitude of the displacement, the cosine and sine signals are squared, added together, and finally the square root is taken, giving the magnitude of the sum of the two vectors. The direction of displacement is determined by comparing the magnitude of the averaged $i_1 \times \sin(2\pi f_s)$ and $i_7 \times \sin(2\pi f_s)$ signals. When the signal associated with i_7 is larger, the sign of the x-direction displacement is positive, because the larger airgap of coil 7 causes the inductance to decrease and the current to increase compared to the current in coil 1. A similar procedure is used for the y-direction, instead using coils 4 and 10.

5.5 Current control

As seen in the equations for suspension forces, the force generated by the coils is proportional to the corresponding suspension control current. As a result, the controller design is simplified if a current command can be sent to the coils instead of a voltage command. This does require slightly more complicated power electronics, as the high inductance of the system requires closed-loop current control. The circuit for each coil has an associated inductance and resistance, where the inductance of the coil L is about 5 mH when the rotor is centered in the airgap, but does change based on rotor position. The resistance R is the resistance of the power resistor connected in series with the coil, where in this system $R = 2.2\ \Omega$, used to measure the winding current. This gives a transfer function of voltage input to the winding

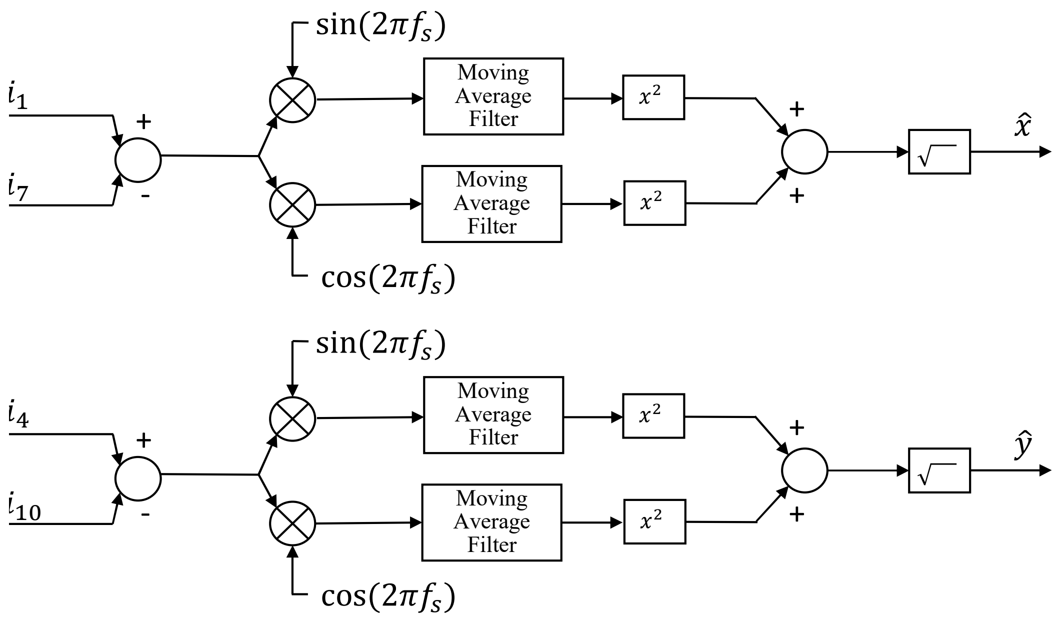

Figure 5.6: Block diagram for demodulation against high-frequency signal

circuit to voltage across the power resistor V_r of

$$\frac{\mathrm{V_r}(s)}{\mathrm{V}(s)} = \frac{R}{Ls + R}. \tag{5.6}$$

The actual current controller implementation can be accomplished either digitally or via an analog circuit. Due to the high bandwidth current control needed to reliably generate the 2 kHz sensing signal, an analog current control board is necessary for this design. An OPA549 board designed for current control has been chosen for initial testing. A custom PCB for current control has also been designed, but has not yet been implemented on the SSBM system.

5.5.1 OPA549 constant current mode board

The PCB selected for analog current control allows high power current generation using the OPA549 chip. The gain of the board is $\frac{1\mathrm{A}}{1\mathrm{V}}$, so for every 1 V input to the circuit it outputs 1 A. A picture of the board is shown in Figure 5.7.

To measure the voltage of the winding as is needed for the airgap estimation an instrumentation amplifier (AD629ANZ) reduces the high common-mode voltage of the winding terminals, producing a signal within the allowable input range of the cRIO.

Figure 5.7: OPA549 PCB for current control

5.5.2 Custom current control PCB design

An alternative current control circuit to the above PCB has also been largely developed, and its full implementation is being considered future work for the purposes of this discussion. The design of this current control PCB follows in this section.

The fundamental circuit for the current feedback loop is shown in Figure 5.9a, and the corresponding transfer functions for each portion of the circuit are given

Table 5.1: Current control PCB resistor and capacitor values

R_1	1 kΩ
R_2	3 kΩ
R_3	1 kΩ
R_4	3 kΩ
C_1	0.1 μC
R_5	1 kΩ
C_2	0 μC
R_6	1 kΩ
C_3	0 μC
R_7	1 kΩ
R_8	9.1 kΩ

in Figure 5.9b. The purpose of this board is to provide a configurable option for closing the current control loop with fully adjustable controller parameters to make the board adaptable to a wide range of systems. The first op-amp takes the difference of V_{in} and V_s and adds a gain of $\frac{R_2}{R_1}$. The next op-amp is connected as a lead filter with a transfer function of the form shown in Figure 5.9b. The third op-amp was added as an optional second filter. For this system the capacitors C_2 and C_3 are not added, and resistors of equal value are used for R_5 and R_6, making this op amp simply an inverting buffer. The power amplifier adds an additional gain and allows a large output current to drive the motor windings. The power amplifier for this board is the OPA541, and each of the smaller op-amps are LM741. The inductance L and resistance R_s in Figure 5.9a are external to the PCB and represent the winding system, and V_{in} and V_s are taken as inputs to the board. For this system, assuming $L = 5$ mH for a centered rotor and $R = 3.2\ \Omega$ the resistor and capacitor values are chosen as in Table 5.1, which gives the loop shape shown in Figure 5.10. The crossover frequency of 9.2 kHz and phase margin of 87° are more than sufficient to reliably produce the 2 kHz sensing signal required for the airgap estimation.

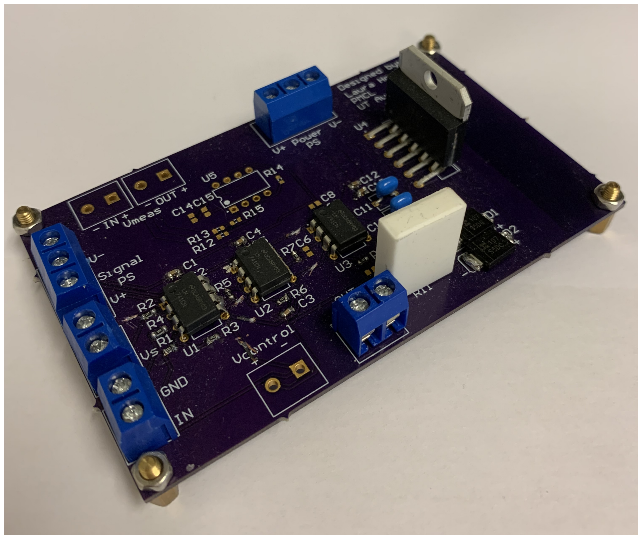

Figure 5.8: Picture of preliminary custom current control PCB

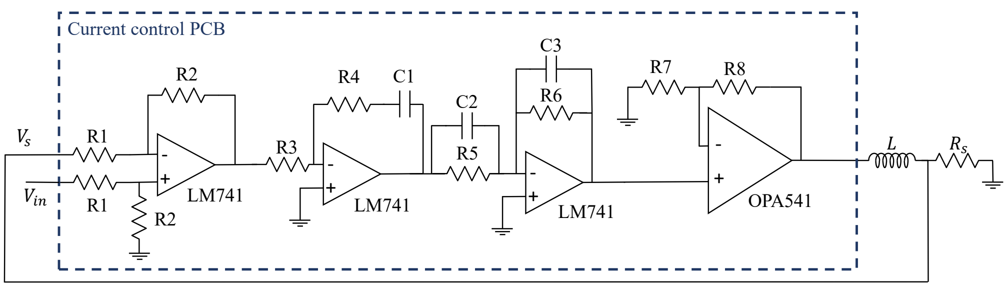

(a) Current control circuit

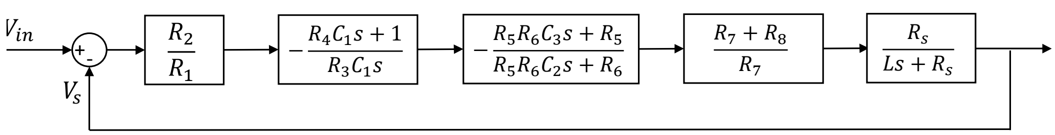

(b) Current control transfer functions

Figure 5.9: Current control PCB circuit with corresponding transfer functions.

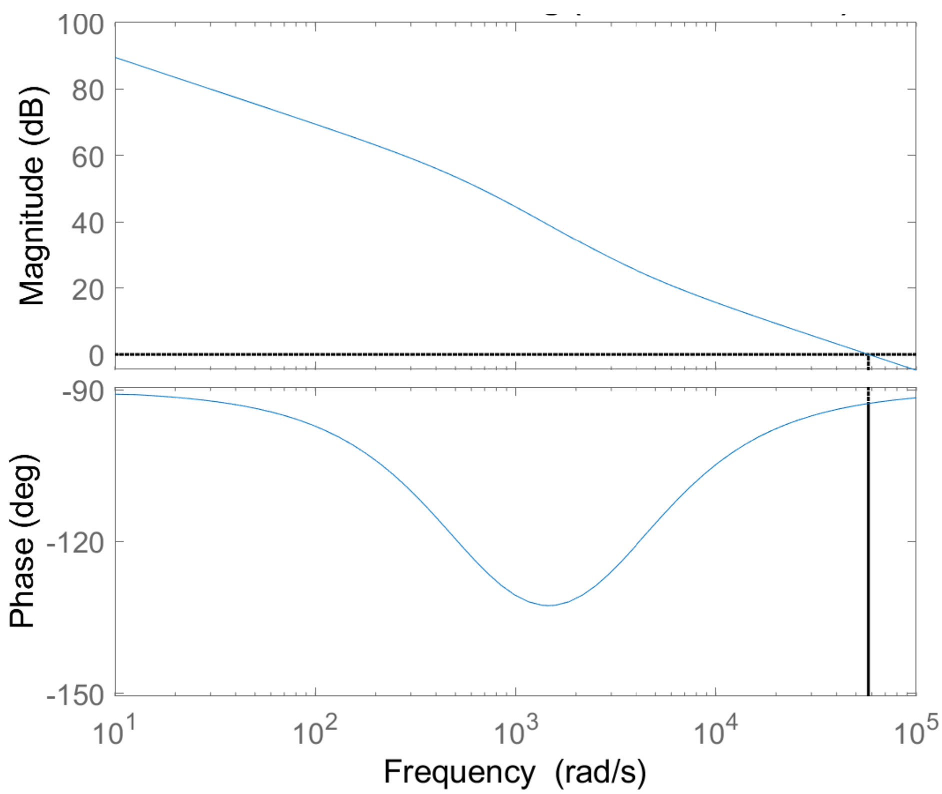

Figure 5.10: Current control bode plot. Component values given in Table 5.1 with approximate coil inductance of 5 mH and resistance of 3 Ω gives bandwidth of 5.8×10^4 rad/s or 9.2 kHz with a phase margin of 87°. Even with variable coil inductance due to rotor position this is a sufficient bandwidth.

5.6 Summary

This chapter discussed the details of the control and estimation design for the SSBM prototype. First the suspension control was developed to stabilize the magnetic suspension of the rotor, followed by an explanation of the torque command generation. The system can be run with either the winding voltage or current as the input. Suspension control and airgap estimation has been developed for the system under voltage control. Current control has not been implemented for the SSBM prototype, but an approach to add this functionality was discussed. One commercially available PCB for current control has been identified, and another custom PCB has been designed which would provide the bandwidth necessary to produce the 2 kHz carrier signal. The next chapter will discuss the results of FEM simulation for both the voltage and current controlled system, and will discuss the experimental results of the estimation implementation.

Chapter 6

Experimental Evaluation

To investigate the effectiveness of this approach for airgap estimation the system was evaluated using finite element simulation in ANSYS Maxwell and initial testing on the constructed testbed. The FE simulation was conducted for the system under both voltage and current control, but up to this point the physical system has only been tested under voltage control. Current control testing of the bearingless motor testbed is a part of the future work.

6.1 Finite element simulation

ANSYS Maxwell is used for finite element simulation of the SSBM system. Figure 6.1 shows the SSBM model in ANSYS. In the first simulation, the voltage is input to the system, and in the second the current is input according to the winding diagram in Figure 3.9. A four-pole magnetic field is generated to produce a torque on the rotor, and a two-pole magnetic field generates suspension force. The simulation is run for four different static displacements of the rotor, 0 mm, 0.25 mm, 0.5 mm, and 0.75 mm. Suspension feedback control is not implemented, so the suspension field is not dependent on rotor displacement. A carrier signal with a frequency of 2 kHz is included in the four coils aligned with the x- and y-axes, labeled coils 1, 4, 7, and 10 in Figure 6.1. The output current or voltage of these four coils is then processed in MATLAB using the demodulation script in Appendix A to find the estimation result.

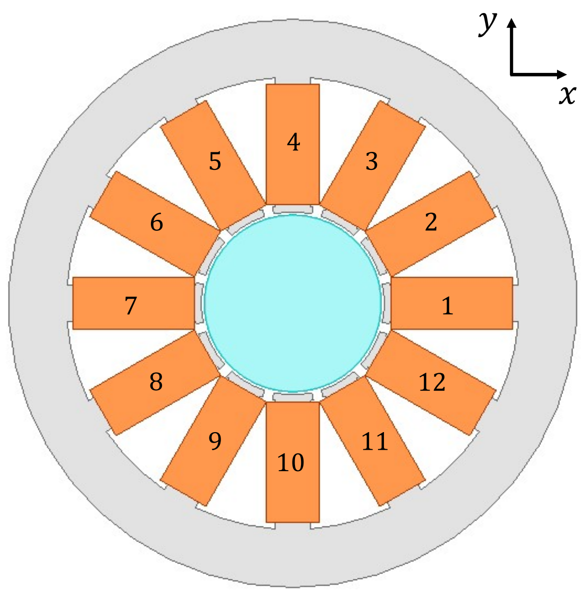

Figure 6.1: Image of SSBM in ANSYS Maxwell with coil numbers

6.1.1 Voltage control

The initial input parameters for the voltage control simulation are as follows: the 3-phase suspension voltage has an amplitude of 10 V and a frequency of 60 Hz, the 3-phase rotation voltage has an amplitude of 20 V and a frequency of 60 Hz, and the carrier signal has an amplitude of 5 V with a frequency 2 kHz.

In order to see a significant variation of coil current with respect to the rotor displacement, the carrier signal must have a large amplitude. Figure 6.3 shows the result where the carrier signal was too small to have a discernible effect. The winding circuit under voltage control effectively acts as a low-pass filter, where the magnitude of the high-frequency response drops off significantly. This can be seen in the power spectrum plot in Figure 6.2. There is a difference in magnitude at 2 kHz depending on rotor displacement, but the value is so small that it does not provide a good basis for airgap estimation.

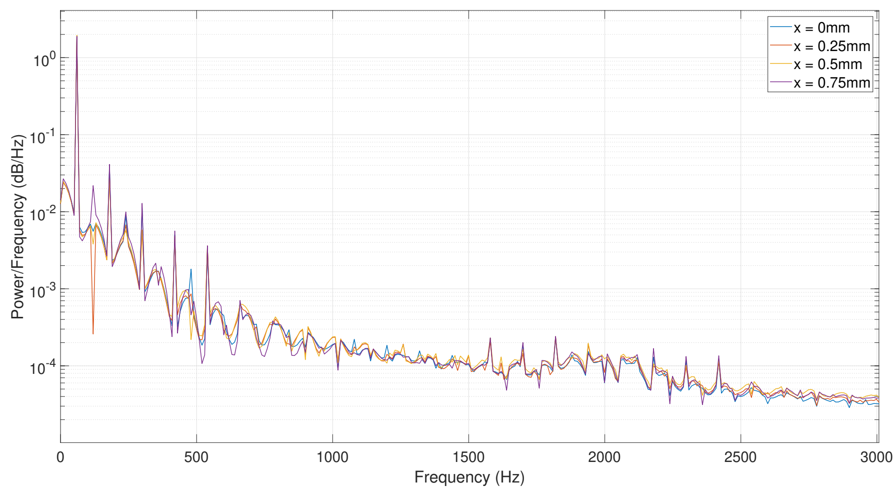

(a) Full frequency range. Largest peak at 60 Hz, frequency of suspension and rotation fields

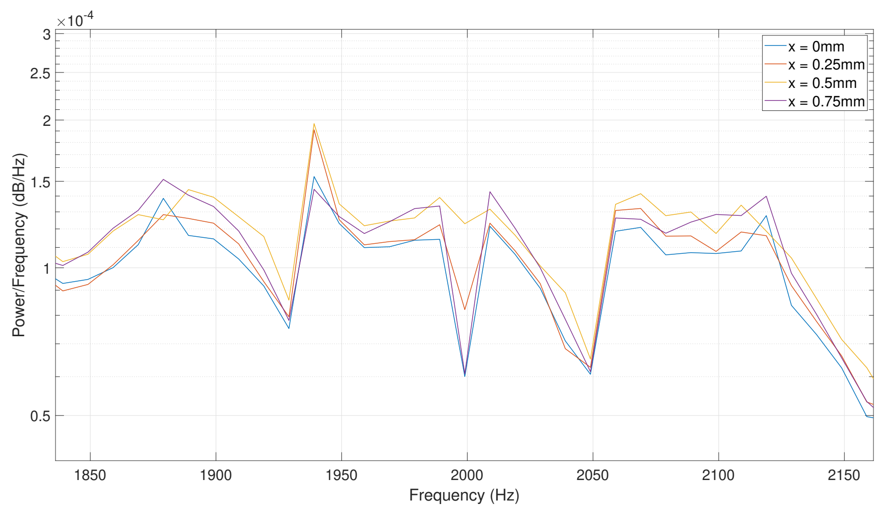

(b) Zoomed in power spectrum centered on 2 kHz, the frequency of the carrier signal

Figure 6.2: Power spectrum for current output of voltage control FEM

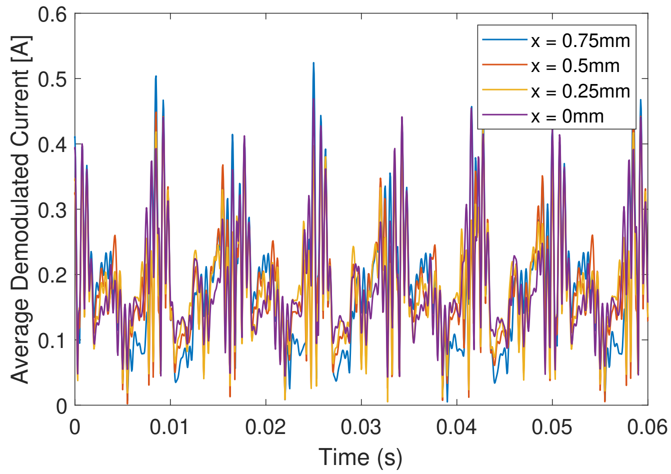

Figure 6.3: FEM estimation results under voltage control with carrier signal amplitude of 5 V

An interesting result from this simulation can be seen in Figure 6.4, where there is a clear variation in the magnitude of the 120 Hz component of the current signal with rotor displacement. This is further illustrated in Figure 6.5, where instead of using the 2 kHz carrier signal for the demodulation of the current, a signal with frequency 120 Hz is used instead. This suggests that the interaction of the stator rotation and suspension fields is acting as a sort of carrier signal for the changing coil inductance, giving an estimate for the rotor displacement when the output current is demodulated against that same frequency.

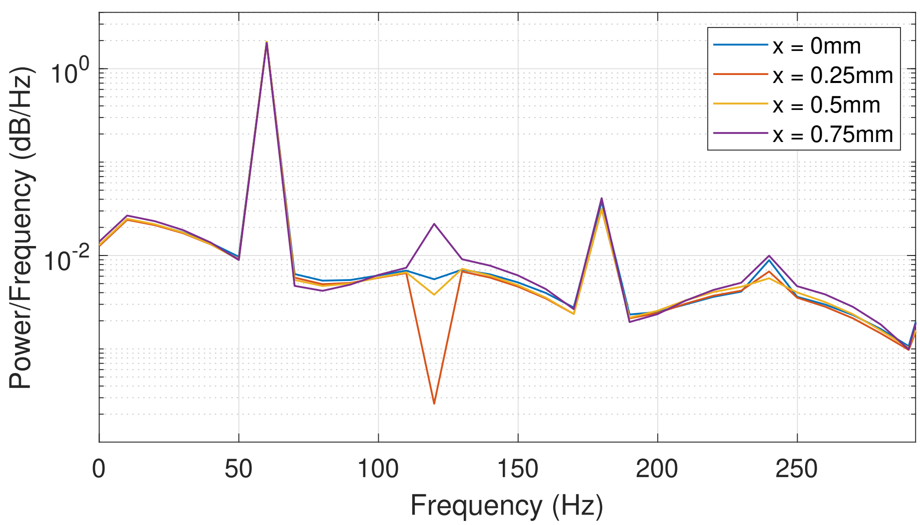

Figure 6.4: Power spectrum zoomed in on 120 Hz

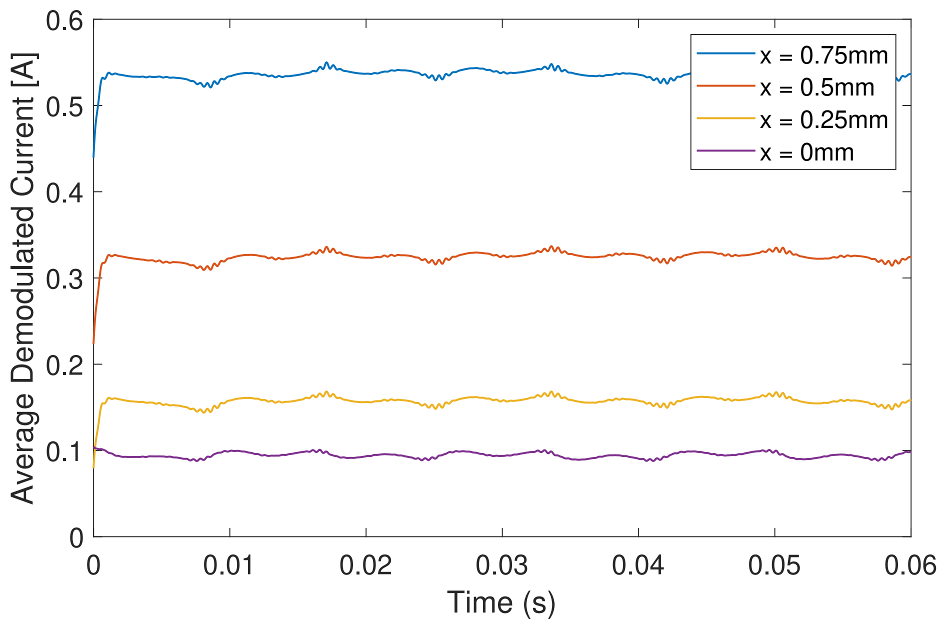

Figure 6.5: FEM estimation results under voltage control with carrier signal amplitude of 5 V, demodulated at 120 Hz

6.1.2 Current control

The same model in ANSYS Maxwell was modified to provide a current input to the windings and take the voltage of the windings as the system's output. As is expected, the variation of coil voltage with rotor displacement is more significant than the variation seen in the coil current for the system under voltage control. The raw voltage signals from ANSYS are shown in Figure 6.6. Examining the difference between the voltage in coil 1 and coil 7, there is a clear change in magnitude for the various rotor positions.

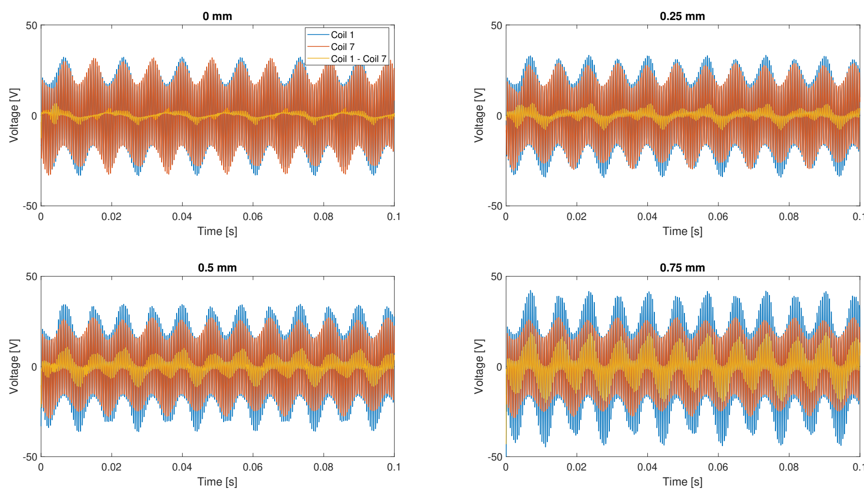

Figure 6.6: Raw voltage signals from FEM under current control under varying rotor eccentric displacement

When these voltage signals are demodulated against the 2 kHz carrier frequency according to the procedure discussed in Chapter 5, the estimation result is as shown in Figure 6.7. The 60 Hz fluctuations in the estimation result are caused by the 60 Hz suspension and rotation fields. Additional filtering could be added to modify the frequencies present in the result, but this plot demonstrates the effectiveness of this approach when the system is under current control.

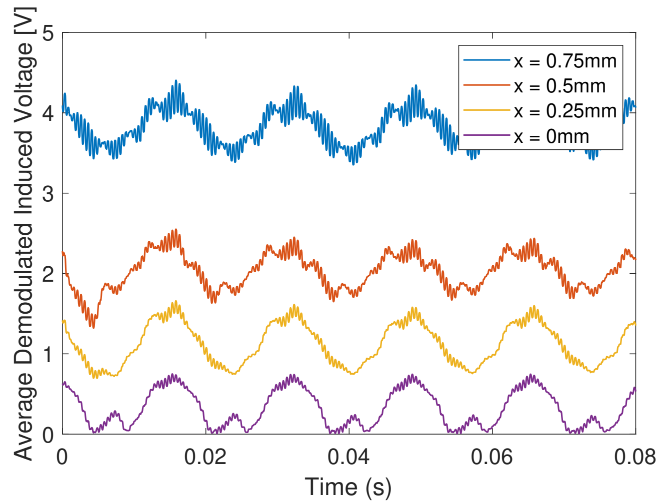

Figure 6.7: FEM estimation results under current control

The torque output of the SSBM is simulated under current control. For the rotation current of amplitude 1 A, the average torque is 16.2 mNm, shown in Figure 6.8.

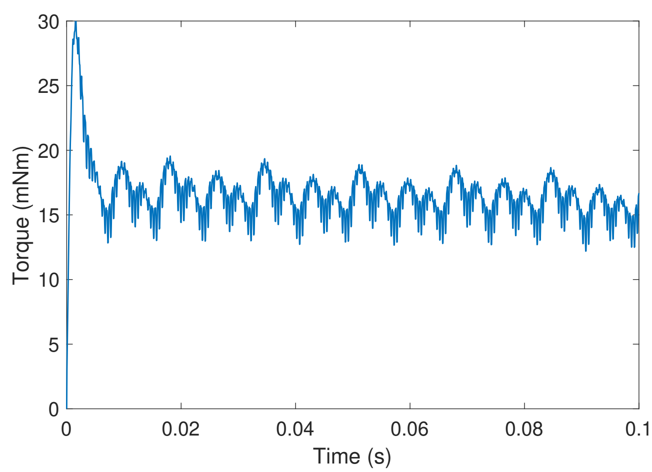

Figure 6.8: FEM torque output under current control

6.2 Bearingless motor platform experimental evaluation

In order to test the estimation technique using the SSBM prototype, stable suspension control needs to be implemented. Loop shaping was used to determine the controller parameters for the system under voltage control. Initial parameters were used to stabilize the system enough to measure the plant's frequency response. The measured plant frequency response and designed loop shape are shown in Figure 6.9, and the selected controller parameters are given in Table 6.1. This controller gives a theoretical bandwidth of 30 Hz in the x-direction and 28 Hz in the y-direction, with sufficient phase margin in both controlled degrees of freedom.

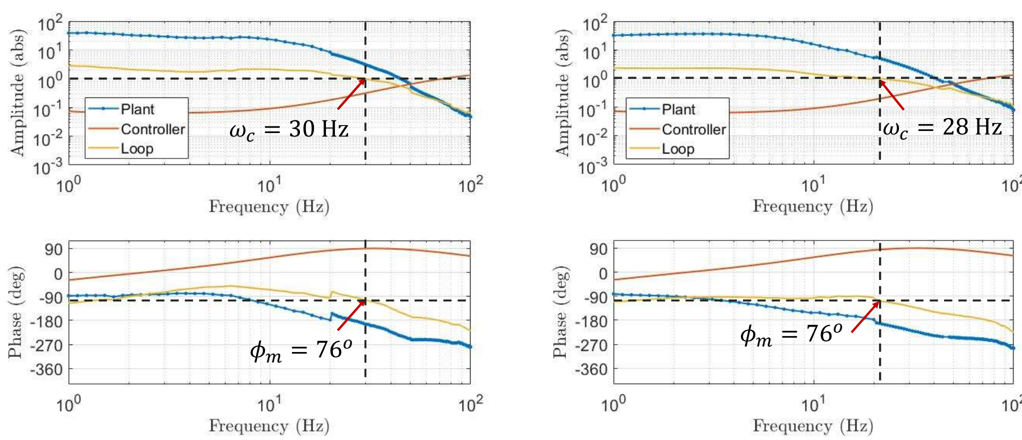

(a) X-direction (b) Y-direction

Figure 6.9: Suspension control loop shaping bode plots under voltage control

Table 6.1: Suspension controller parameters under voltage control

K_p	0.059
α	6
τ	0.002
T_i	0.22

The measured loop bode plots for both the x- and y-direction of the SSBM prototype under voltage control where the inductive sensors are used for the suspension feedback are shown in Figure 6.10. There is some asymmetry in the system, but the loop dynamics of both DOFs are sufficient for initial testing of the estimation approach.

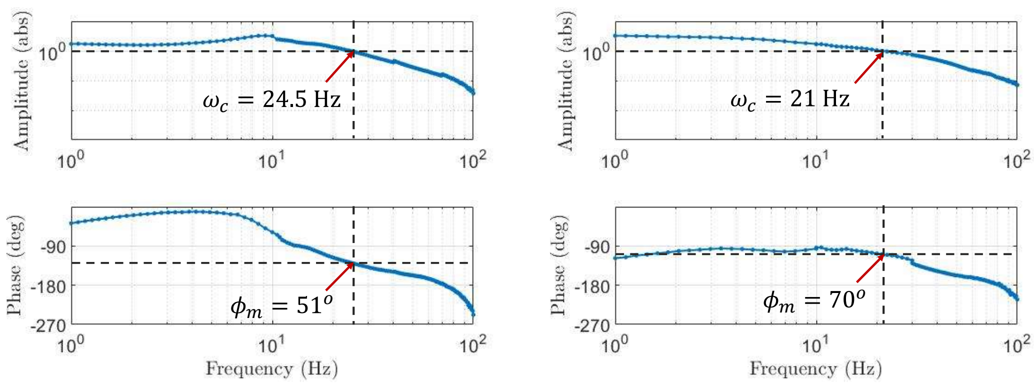

(a) X-direction

(b) Y-direction

Figure 6.10: Measured suspension control loop bode plots under voltage control

6.3 Experimental estimation results

The SSBM testbed was tested under voltage control, but hardware delays have caused current control testing to be pushed to future work. In this section, the results of the estimation process for the system are presented, and the limitations of the system under voltage control are discussed.

6.3.1 Voltage control

Under voltage control, as was demonstrated in the FEM results, it is expected that the estimation performance would not perform well with a small carrier signal. For the following tests, a 0.1 V carrier signal was output from the cRIO, which when amplified by the linear power amplifier of gain 6, translated to an amplitude of

0.6 V for the carrier signal at the coils. In the simulations this was not sufficient to see a response from the estimator, but in the physical system some interaction with the suspension and rotation signals enabled estimation. Figure 6.12 compares the estimated displacement with the reading of the inductive sensors as the rotor is manually displaced, either in the x- or y-direction. When scaled properly, the estimated displacement tracks the sensor output closely. The estimation signal was scaled by changing the gain and offset added to the direct estimation signal, the values of which were determined by visually comparing the estimation signal with the sensor signals. In future, this process could be improved and a more deterministic method could be developed to find the relationship between demodulated current and rotor position. Figure 6.11 shows the estimator performance for a sinusoidal reference in the x-direction. The estimated position leads the measured value, which will need to be addressed when using the estimate for the suspension feedback, but does provides a good estimate of the amplitude.

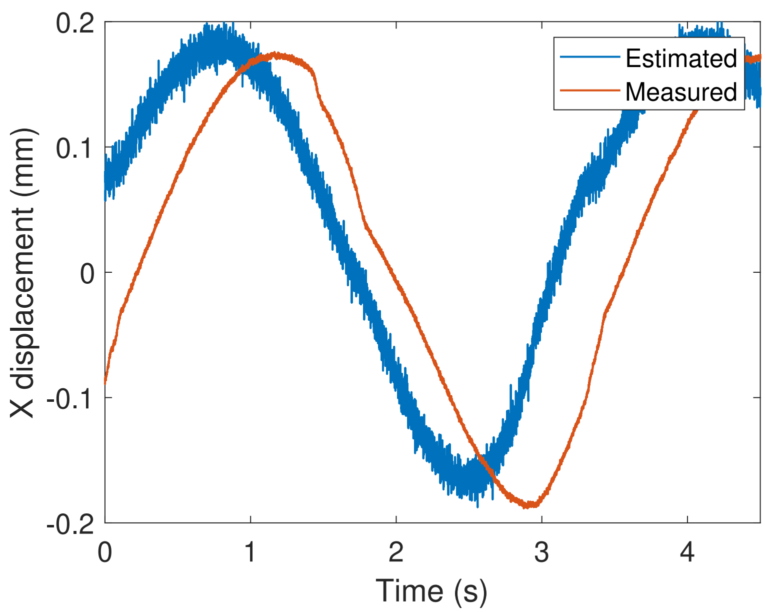

Figure 6.11: Estimator performance for 0.3 Hz sinusoidal position reference in the x-direction

6.4 Summary

In summary, the high-frequency carrier signal estimation method was tested on a hysteresis bearingless motor using both FE simulation and the constructed testbed. The FE simulations were conducted using ANSYS Maxwell, where the system was modeled for both voltage and current control. The voltage control simulation did not give a good airgap estimation result based on the 2 kHz carrier signal, but the 120 Hz component of the current did have some relationship to the rotor displacement. FE simulation using current control gave better estimation results, where a clear variation in demodulated voltage could be seen for different rotor positions. The physical testbed has so far only been evaluated under voltage control. When the rotation and suspension fields are added to the carrier signal, the estimate of rotor displacement closely follows the sensor signal for both the x- and y-directions. It is expected that the estimation result would be improved if current control was used, and that the estimation would be possible even when the rotation and suspension signals were turned off.

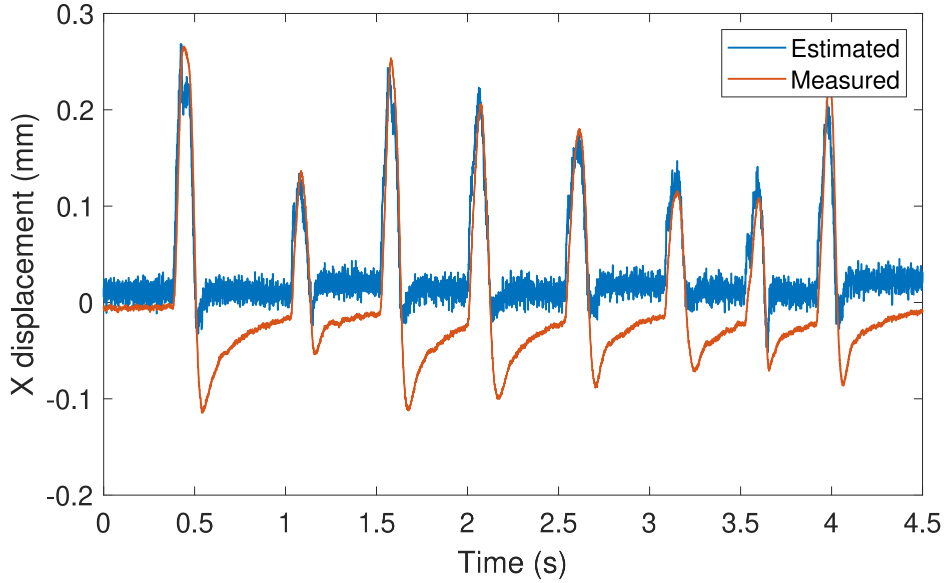

(a) X-direction displacement

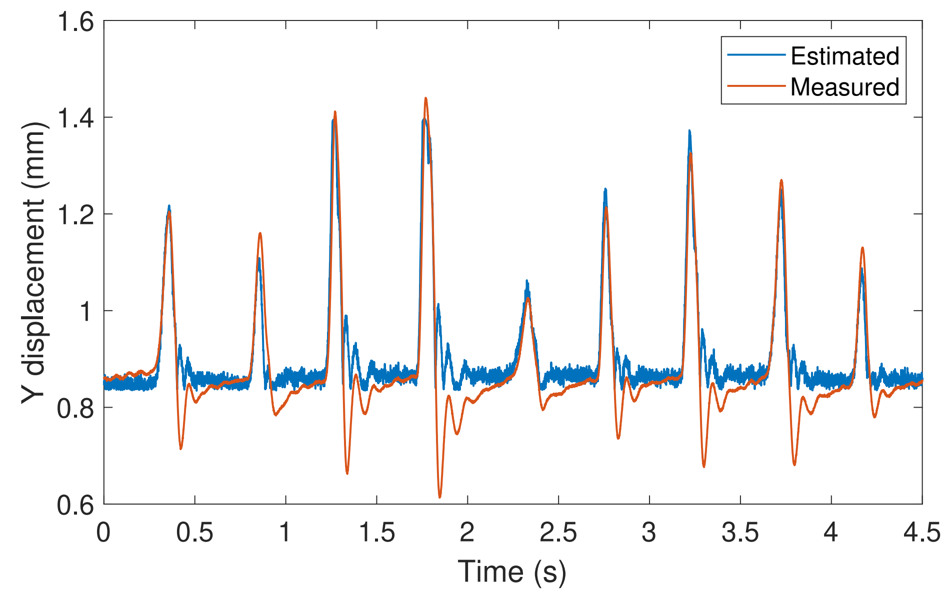

(b) Y-direction displacement

Figure 6.12: Estimator response to manual disturbance

Chapter 7

Conclusion and Future Work

7.1 Conclusion

To conclude, this thesis has presented the design and preliminary testing of a self-sensing bearingless hysteresis-type motor where the airgap estimation is enabled by the injection of a high-frequency carrier signal to amplify the variation of winding voltage with rotor displacement. Contributions of this work include:

1. Developed an analytical model for the bearingless hysteresis motor. Described the relationship between stator winding inductance and airgap length to enable self-sensing. Demonstrated the operating principle using a single degree-of-freedom system and an analytical model of the SSBM.

2. Designed suspension controllers and estimation procedures for the self-sensing motor system. Developed a PCB for analog current control to improve estimation performance.

3. Designed and constructed a testbed for a self-sensing bearingless hysteresis motor.

4. Simulated motor and estimation performance for both voltage and current controlled system. Evaluated airgap estimation for voltage controlled stator windings on the constructed testbed.

The presented results demonstrate the feasibility of airgap estimation for a bearingless hysteresis motor using a high-frequency carrier signal and the response of the stator windings. Simulation results are promising for improved estimation performance when current control is implemented on the SSBM testbed. With the system under voltage control the airgap estimation is highly dependent on the suspension signals, but under current control the high-frequency carrier signal itself should enable the estimation. The bandwidth for suspension control was sufficient for initial testing, but would likely also be improved by controlling the current in the windings.

7.2 Future Work

7.2.1 Improvement of current prototype

So far this project has demonstrated the feasibility of this approach and simulated improved airgap estimation using current controlled stator windings. Immediate next steps for this project will focus on implementing current control for the current testbed, using both the OPA549 current-mode boards and the custom designed PCBs for current control as presented in Chapter 5.

For the experiments presented in this thesis, the sensor signals were used to enable feedback control for the rotor suspension. Once the airgap estimation is improved using current controlled stator windings, the suspension control system will be modified to use the estimated values as the feedback signal instead, making the testbed motor fully operational without the use of external position sensors.

7.2.2 Suggestions for future development

Hysteresis motors are a promising technology for ultra-high-speed drives because of their simple construction and the high mechanical strength of the rotor. Coupled with frictionless, low-maintenance bearingless motor operation these machines would be especially well suited to high-speed applications such as flywheel energy storage systems. This thesis presents a way to make these systems more cost effective and robust by eliminating the need for airgap sensors, but the transient dynamics of hysteresis motors are not well understood. Better models of these machines could enable optimized design for bearingless hysteresis motors.

Appendix A

MATLAB Code

A.1 Demodulation function

This function takes signals from two windings to find the estimated displacement in a particular direction x, where `v_1` is from the coil aligned with the positive x-axis, and `v_2` is from the coil aligned with the negative x-axis. These signals can be either winding voltage or current. A vector of time values, `t`, carrier frequency, `f`, and moving average window size, `n` are also taken as inputs. The function returns two vectors of the same length as `v_1` and `v_2`, `r_mag` for the magnitude of the estimate, and `r_phase` for the phase. This demodulation function was used for both the analytical modeling and processing the results from FEM simulation in ANSYS Maxwell.

```
function [r_mag, r_phase] = Demod_fun(v_1, v_2, t, f, n)
r1_sin = v_1.*(sin(f*2*pi*t)');
r2_sin = v_2.*(sin(f*2*pi*t)');
r1_cos = v_1.*(cos(f*2*pi*t)');
r2_cos = v_2.*(cos(f*2*pi*t)');

amp_sin_1 = movmean(r1_sin,n,'Endpoints','fill');
amp_cos_1 = movmean(r1_cos,n,'Endpoints','fill');
amp_sin_2 = movmean(r2_sin,n,'Endpoints','fill');
amp_cos_2 = movmean(r2_cos,n,'Endpoints','fill');

```

```
amp_sin = amp_sin_1 - amp_sin_2;
amp_cos = amp_cos_1 - amp_cos_2;

r_mag = sqrt(amp_sin.^2 + amp_cos.^2);
r_phase = [amp_sin, amp_cos];
end
```

A.2 Analytical modeling

A.2.1 Voltage control simulation

```
dt = 5e-5;              %time step size [s]
T = 0.1;                %simulation end time [s]

mu_0 = 4*pi*1e-7;       %permeability of air
R_rotor = 24.75e-3;     %rotor radius
R = R_rotor + 1e-3/2;
g0 = 1e-3;              %nominal air gap
l_rotor = 10e-3;
res = 2.2;              %resistance
Res = res*eye(12);      %resistance matrix

N_turns = 200;          %number of turns in winding
n_slots = 12;           %number of stator slots
N_sample = 12*20;       %total number of samples (20 per slot)

Vr = 20;                %rotation voltage amplitude [V]
Vs = 10;                %suspension voltage amplitude [V]
Vsense = 10;
f = 60;

phi = linspace(0,2*pi,N_sample); %vector of angle for each spatial
    sample
N_data = floor(T/dt+1); %number of timesteps
n = 12;                 %system dimension

```

```
result = zeros(N_data,4);

for xx = 1:4

    x = (xx-1)*0.25e-3;
    y = 0;

    %Carter's coefficient:
    tau = 2*pi/12*R;
    b0 = 4.573e-3;
    h = 4/pi*(b0./(2*g0).*atan(b0./(2*g0)) - log(sqrt(1+(b0./(2*g0
        )).^2)));
    Kc = tau./(tau - h.*g0);

    g0eff = Kc.*g0; %effective nominal gap with Carter's
        coefficient
    R = R - (Kc - 1).*g0; %modified radius
    g = g0eff - x*cos(phi) - y*sin(phi); %actual gap length
    geff = g;

    tt = linspace(0,T,N_data);  %vector for time
    ii = zeros(n,N_data);   %matrix for current data
    ll = zeros(n,N_data);   %matrix for flux linkage data
    vu = zeros(n,N_data);   %matrix for voltage data

    i0 = zeros(12,1);

    N_stator = zeros(N_sample,n_slots);
    for k = 1:n_slots
        %fill in MMF space distribution
        N_stator(floor((k-1)*N_sample/n_slots)+1:floor(k*N_sample/
            n_slots),k) = N_turns;
    end

    %% Simulation
    for i = 1:N_data
        t = tt(i);

```

```
        %Set-up stator voltages
        va = Vr*cos(4*f*pi*t);
        vb = Vr*cos(4*f*pi*t - 2*pi/3);
        vc = Vr*cos(4*f*pi*t + 2*pi/3);
        vu = Vs*cos(2*f*pi*t + 2*pi/24);
        vv = Vs*cos(2*f*pi*t + 2*pi/24 - 2*pi/3);
        vw = Vs*cos(2*f*pi*t + 2*pi/24 + 2*pi/3);
        vsense = Vsense*cos(2*pi*2000*t);

        uu(1,i) = va - vu + vsense;
        uu(2,i) = -vc + vw;
        uu(3,i) = vb + vw;
        uu(4,i) = -va - vv - vsense;
        uu(5,i) = vc - vv;
        uu(6,i) = -vb + vu;
        uu(7,i) = va + vu + vsense;
        uu(8,i) = -vc - vw;
        uu(9,i) = vb - vw;
        uu(10,i) = -va + vv - vsense;
        uu(11,i) = vc + vv;
        uu(12,i) = -vb - vu;

        %Inductance
        for j = 1:n_slots
            n_stator_1 = N_stator(:,j);
            V = 200/12; %rotor potential

            for k = 1:n_slots
                M_stator = N_stator(:,k) - V; %flux = P*(A - V)
                L_SS(j,k) = mu_0*l_rotor*trapz(phi,R'.*n_stator_1
                    .*M_stator./geff');
            end
        end
        %calculate current
        ii(:,i) = (L_SS+Res)\(uu(:,i)*dt + i0);
        %save previous current values
        i0 = ii(:,i);
    end
```

```matlab
%         result(:,xx) = ii(1,:)' - ii(7,:)';
     result(:,xx) = Demod_fun(ii(1,:)',ii(7,:)', tt, 2000, 10);
%      result(6:997,xx) = highpass(result(6:997,xx),500,20e3);
end

%% Plot results
figure
plot(tt,result(:,4),tt,result(:,3),tt,result(:,2),tt,result(:,1))
legend( 'x = 0.75mm','x = 0.5mm','x = 0.25mm', 'x = 0mm')

xlabel('Time (s)')
ylabel('Average Demodulated Current [A]')
```

A.2.2 Current control simulation

```matlab
dt = 5e-5;                 %time step size [s]
T = 0.1;                   %simulation end time [s]

mu_0 = 4*pi*1e-7;          %permeability of air
R_rotor = 24.75e-3;        %rotor radius [m]
R = R_rotor + 1e-3/2;      %radius through center of airgap [m]
g0 = 1e-3;                 %nominal air gap [m]
l_rotor = 10e-3;           %rotor axial length [m]

N_turns = 200;             %number of turns in winding
n_slots = 12;              %number of stator slots
N_sample = 12*20;          %total number of samples (20 per slot)

Ir = 1;                    %rotation current amplitude [A]
Is = 0.1;                  %suspension current amplitude [A]
Isense = 0.2;              %carrier signal amplitude [A]
f = 60;                    %frequency of rotation and suspension currents [Hz]

phi = linspace(0,2*pi,N_sample); %vector of angle for each spatial sample
N_data = floor(T/dt+1); %number of timesteps
```

```
n = 12;                    %system dimension

result = zeros(N_data,4);

for xx = 1:4
    %run simulation for four values of x: 0, 0.25, 0.5, and 0.75
        mm
    x = (xx-1)*0.25e-3;
    %keep y centered
    y = 0;

    tau = 2*pi/12*R; %arc length
    b0 = 4.573e-3;
    h = 4/pi*(b0./(2*g0).*atan(b0./(2*g0)) - log(sqrt(1+(b0./(2*g0
        )).^2)));
    Kc = tau./(tau - h.*g0); %Carter's coefficient
    g0eff = Kc.*g0; %effective  nominal gap with Carter's
        coefficient
    R = R - (Kc - 1).*g0; %modified radius
    g = g0eff - x*cos(phi) - y*sin(phi); %actual gap length
    geff = g;

    tt = linspace(0,T,N_data);  %vector for time
    ii = zeros(n,N_data);   %matrix for current data
    ll = zeros(n,N_data);   %matrix for flux linkage data
    uu = zeros(n,N_data);   %matrix for voltage data

    lambda0 = zeros(12,1);

    N_stator = zeros(N_sample,n_slots);
    for k = 1:n_slots
        %fill in MMF space distribution
        N_stator(floor((k-1)*N_sample/n_slots)+1:floor(k*N_sample/
            n_slots),k) = N_turns;
    end

    %% Simulation
    for i = 1:N_data
```

```
        t = tt(i);

        %Set-up currents
        ia = Ir*cos(4*f*pi*t);
        ib = Ir*cos(4*f*pi*t - 2*pi/3);
        ic = Ir*cos(4*f*pi*t + 2*pi/3);
        iu = Is*cos(2*f*pi*t + 2*pi/24);
        iv = Is*cos(2*f*pi*t + 2*pi/24 - 2*pi/3);
        iw = Is*cos(2*f*pi*t + 2*pi/24 + 2*pi/3);
        isense = Isense*cos(2*pi*2000*t);

        ii(1,i) = ia - iu + isense;
        ii(2,i) = -ic + iw;
        ii(3,i) = ib + iw;
        ii(4,i) = -ia - iv - isense;
        ii(5,i) = ic - iv;
        ii(6,i) = -ib + iu;
        ii(7,i) = ia + iu + isense;
        ii(8,i) = -ic - iw;
        ii(9,i) = ib - iw;
        ii(10,i) = -ia + iv - isense;
        ii(11,i) = ic + iv;
        ii(12,i) = -ib - iu;

        %Inductance
        for j = 1:n_slots
            n_stator_1 = N_stator(:,j);
            V = 200/12; %rotor potential
            for k = 1:n_slots
                M_stator = N_stator(:,k) - V; %flux = P*(A - V)
                L_SS(j,k) = mu_0*l_rotor*trapz(phi,R'.*n_stator_1
                    .*M_stator./geff');
            end
        end

        %flux linkage
        lambda = L_SS*ii(:,i);
        %voltage
```

```
        uu(:,i) = (lambda - lambda0)/dt + 0.1*ii(:,i);
        %save previous flux linkage values
        lambda0 = lambda;
    end

    %demodulate voltage output
    result(:,xx) = Demod_fun(uu(1,:)',uu(7,:)', tt, 2000, 10);
end

%% Plot results
figure
plot(tt,result(:,4),tt,result(:,3),tt,result(:,2),tt,result(:,1))
legend( 'x = 0.75mm','x = 0.5mm','x = 0.25mm', 'x = 0mm')

xlabel('Time (s)')
ylabel('Average Demodulated Induced Voltage [V]')
```

A.3 Processing FEM results

MATLAB was used to demodulate the winding data from simulation to give a simulated estimate of rotor displacement. This script is as follows:

```
%read matrices containing data for all coils for four rotor positions
d0 =  readmatrix('VC_04_16_22_0um.csv');
d25 =  readmatrix('VC_04_16_22_250um.csv');
d5 =  readmatrix('VC_04_16_22_500um.csv');
d75 =  readmatrix('VC_04_16_22_750um.csv');

%set simulation parameters
Fs = 1/5e-5; %Hz, sampling frequency
t = 0:1/Fs:.1; %s, time at sampling frequency
f = 2000; %Hz, carrier frequency

%rename
d00_1 = d0(:,2);      % coil number 1
d50_1 = d5(:,2);
```

```
d25_1 = d25(:,2);
d75_1 = d75(:,2);
d00_7 = d0(:,8);      % coil number 7
d50_7 = d5(:,8);
d25_7 = d25(:,8);
d75_7 = d75(:,8);

%% Spectrum plotting

[freq00, Diff_00_Spectrum] = Spectrum_Cal(d00_1-d00_7, Fs);
[freq25, Diff_25_Spectrum] = Spectrum_Cal(d25_1-d25_7, Fs);
[freq50, Diff_50_Spectrum] = Spectrum_Cal(d50_1-d50_7, Fs);
[freq75, Diff_75_Spectrum] = Spectrum_Cal(d75_1-d75_7, Fs);

figure
semilogy(freq00, Diff_00_Spectrum)
hold on
semilogy(freq25, Diff_25_Spectrum)
semilogy(freq50, Diff_50_Spectrum)
semilogy(freq75, Diff_75_Spectrum)
legend('x = 0mm','x = 0.25mm','x = 0.5mm','x = 0.75mm')
grid on
title('Periodogram Using FFT')
xlabel('Frequency (Hz)')
ylabel('Power/Frequency (dB/Hz)')

%% Demod

n = Fs/f; %sampling frequency/carrier frequency
[amp0,phase0] = Demod_fun(d00_1, d00_7, t,f, n);
[amp25, phase25] = Demod_fun(d25_1, d25_7, t,f, n);
[amp50, phase50] = Demod_fun(d50_1, d50_7, t, f,n);
[amp75, phase75] = Demod_fun(d75_1, d75_7, t, f,n);

figure
plot(t, amp75)
hold on
plot(t, amp50)
```

```
plot(t, amp25)
plot(t, amp0)

legend('x = 0.75mm','x = 0.5mm','x = 0.25mm','x = 0mm')
xlabel('Time (s)')
ylabel('Average Demodulated Current [A]')
```

The power spectrum of the winding signal was calculated using the function Spectrum_Cal, where the signal and sampling frequency are input, and vectors for frequency and power spectrum density are returned:

```
function [freq, psdx] = Spectrum_Cal(x, Fs)
N = length(x);
xdft = fft(x);
xdft = xdft(1:N/2+1);
psdx = (1/(Fs*N)) * abs(xdft).^2;
psdx(2:end-1) = 2*psdx(2:end-1);
freq = 0:Fs/length(x):Fs/2;
end
```

Appendix B

LabVIEW Code

The estimation and control for the SSBM prototype was implemented in LabVIEW. This section shows the block diagrams for both the real-time and FPGA portions of the code.

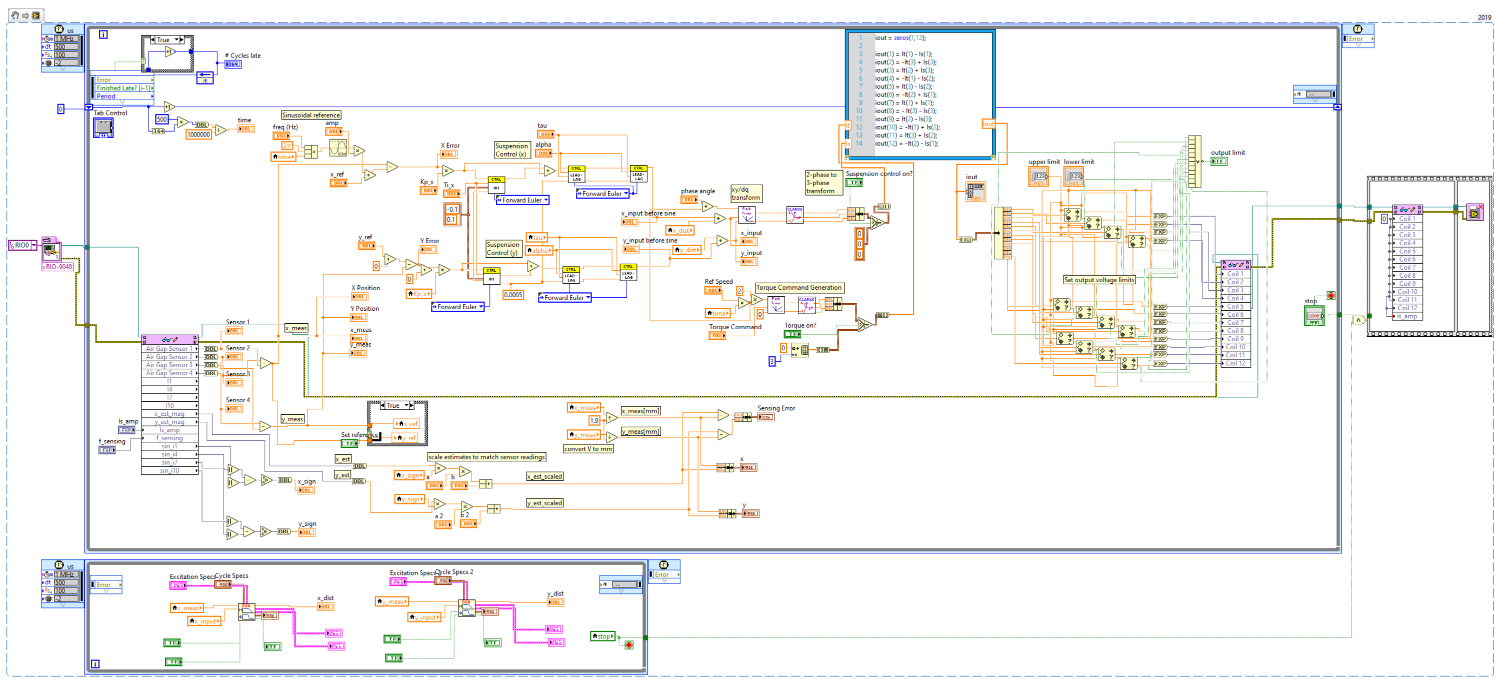

Figure B.1: LabVIEW real-time suspension control block diagram

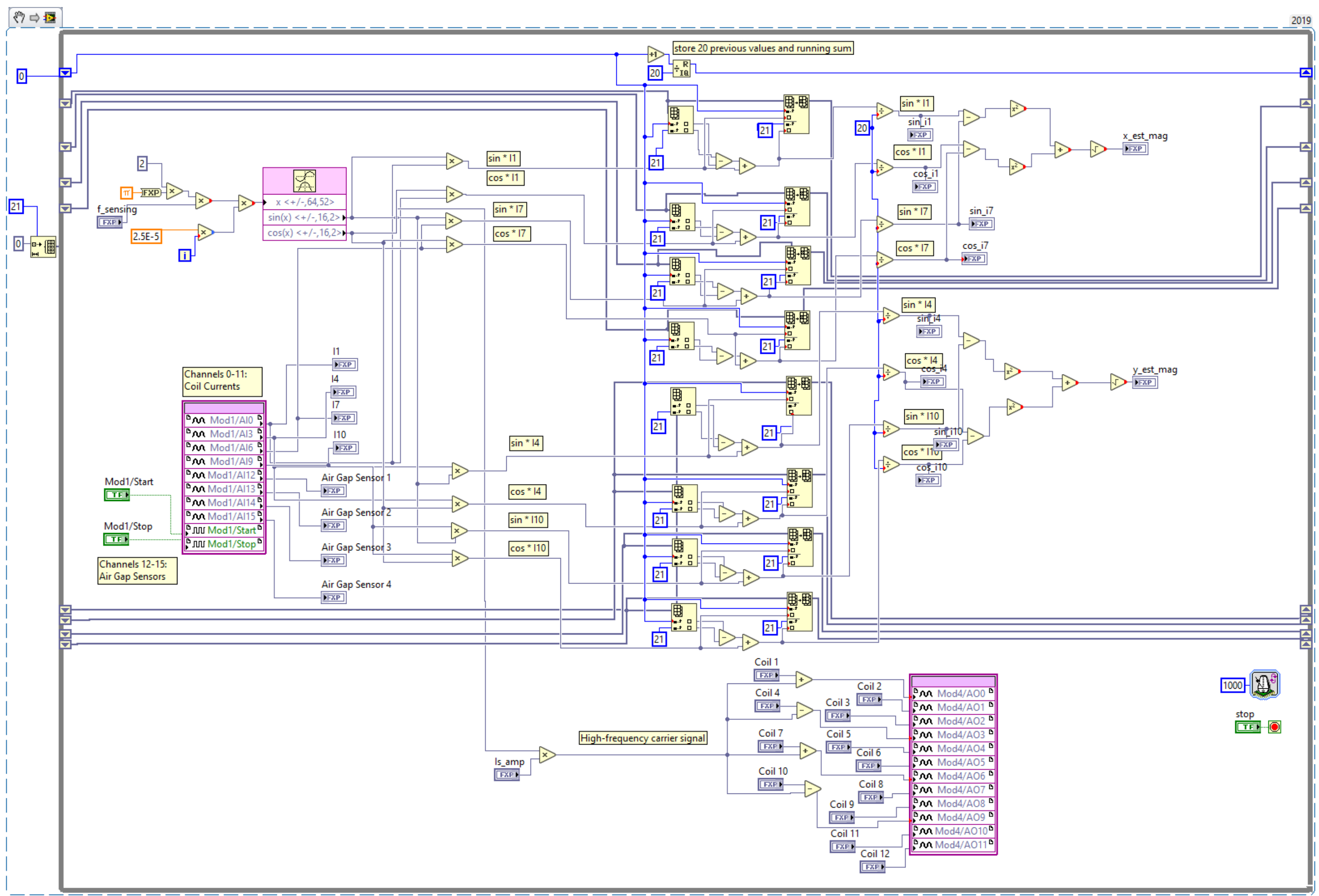

Figure B.2: LabVIEW block diagram of demodulation and carrier signal generation in FPGA

Bibliography

[1] M. Ooshima and C. Takeuchi, "Magnetic suspension performance of a bearingless brushless dc motor for small liquid pumps," *IEEE Transactions on Industry Applications*, vol. 47, no. 1, pp. 72–78, 2010.

[2] P. Puentener, M. Schuck, D. Steinert, T. Nussbaumer, and J. W. Kolar, "A 150 000-r/min bearingless slice motor," *IEEE/ASME Transactions on Mechatronics*, vol. 23, no. 6, pp. 2963–2967, 2018.

[3] J. Chen, J. Zhu, and E. L. Severson, "Review of bearingless motor technology for significant power applications," *IEEE Transactions on Industry Applications*, vol. 56, no. 2, pp. 1377–1388, 2019.

[4] Q. Li, P. Boesch, M. Haefliger, J. W. Kolar, and D. Xu, "Basic characteristics of a 4kw permanent-magnet type bearingless slice motor for centrifugal pump system," in *2008 international conference on electrical machines and systems.* IEEE, 2008, pp. 3037–3042.

[5] M. Ooshima, "Analyses of rotational torque and suspension force in a permanent magnet synchronous bearingless motor with short-pitch winding," in *2007 IEEE Power Engineering Society General Meeting.* IEEE, 2007, pp. 1–7.

[6] M. Ooshima, A. Chiba, T. Fukao, and M. A. Rahman, "Design and analysis of permanent magnet-type bearingless motors," *IEEE Transactions on Industrial Electronics*, vol. 43, no. 2, pp. 292–299, 1996.

[7] C. Barthod and G. Lemarquand, "Design of an actuator being both a permanent magnet synchronous motor and a magnetic suspension," *IEEE transactions on magnetics*, vol. 34, no. 4, pp. 2105–2107, 1998.

[8] J. Asama, T. Asami, T. Imakawa, A. Chiba, A. Nakajima, and M. A. Rahman, "Effects of permanent-magnet passive magnetic bearing on a two-axis actively regulated low-speed bearingless motor," *IEEE Transactions on Energy Conversion*, vol. 26, no. 1, pp. 46–54, 2010.

[9] Y. Okada, S. Miyamoto, and T. Ohishi, "Levitation and torque control of internal permanent magnet type bearingless motor," *IEEE Transactions on Control Systems Technology*, vol. 4, no. 5, pp. 565–571, 1996.

[10] A. Chiba, D. Power, and M. Rahman, "Characteristics of a bearingless induction motor," *IEEE Transactions on Magnetics*, vol. 27, no. 6, pp. 5199–5201, 1991.

[11] E. F. Rodriguez and J. A. Santisteban, "An improved control system for a split winding bearingless induction motor," *IEEE Transactions on Industrial Electronics*, vol. 58, no. 8, pp. 3401–3408, 2010.

[12] J. Chen and E. L. Severson, "Optimal design of the bearingless induction motor for industrial applications," in *2019 IEEE Energy Conversion Congress and Exposition (ECCE)*. IEEE, 2019, pp. 5265–5272.

[13] P. Wu and K. Tseng, "A self-bearing centrifugal blood pump based on induction motor with active and passive magnetic bearings," in *The Fifth International Conference on Power Electronics and Drive Systems, 2003. PEDS 2003.*, vol. 2. IEEE, 2003, pp. 1642–1646.

[14] J. Chen and E. L. Severson, "Design and modeling of the bearingless induction motor," in *2019 IEEE International Electric Machines & Drives Conference (IEMDC)*. IEEE, 2019, pp. 343–350.

[15] L. Zhou, W. Gruber, and D. L. Trumper, "Position control for hysteresis motors: Transient-time model and field-oriented control," *IEEE Trans. on Ind. Appl.*, vol. 54, no. 4, pp. 3197–3207, 2018.

[16] M. Imani Nejad, "Self-bearing motor design & control," Ph.D. dissertation, Massachusetts Institute of Technology, 2013.

[17] H. Ding, H. Zhu, and Y. Hua, "Optimization design of bearingless synchronous reluctance motor," *IEEE Transactions on Applied Superconductivity*, vol. 28, no. 3, pp. 1–5, 2018.

[18] F. Ahmed, D. Saikia, S. Chatterjee, H. Singh, P. Das, and K. Kalita, "Self-bearing switched reluctance motor: A review," in *2012 1st International Conference on Power and Energy in NERIST (ICPEN)*. IEEE, 2012, pp. 1–6.

[19] E. Severson, R. Nilssen, T. Undeland, and N. Mohan, "Analysis of the bearingless ac homopolar motor," in *2012 XXth International Conference on Electrical Machines*. IEEE, 2012, pp. 570–576.

[20] H. Jia, J. Wang, M. Cheng, W. Hua, C. Fang, and Z. Ling, "Comparison study of electromagnetic performance of bearingless flux-switching permanent-magnet motors," *IEEE Transactions on Applied Superconductivity*, vol. 26, no. 4, pp. 1–5, 2016.

[21] H. Bleuler, D. Vischer, G. Schweitzer, A. Traxler, and D. Zlatnik, "New concepts for cost-effective magnetic bearing control," *Automatica*, vol. 30, no. 5, pp. 871–876, 1994.

[22] T. Mizuno and H. Bleuler, "Self-sensing magnetic bearing control system design using the geometric approach," *Control Engineering Practice*, vol. 3, no. 7, pp. 925–932, 1995.

[23] K. Matsuda, S. Kijimoto, and Y. Kanemitsu, "Self-sensing three-pole magnetic bearing using a kalman filter," in *2006 SICE-ICASE International Joint Conference*. IEEE, 2006, pp. 1590–1594.

[24] M. D. Noh and E. H. Maslen, "Self-sensing magnetic bearings using parameter estimation," *IEEE Transactions on Instrumentation and Measurement*, vol. 46, no. 1, pp. 45–50, 1997.

[25] T. Tera, Y. Yamauchi, A. Chiba, T. Fukao, and M. A. Rahman, "Performances of bearingless and sensorless induction motor drive based on mutual inductances and rotor displacements estimation," *IEEE Transactions on Industrial Electronics*, vol. 53, no. 1, pp. 187–194, 2006.

[26] A. Chiba and J. A. Santisteban, "A pwm harmonics elimination method in simultaneous estimation of magnetic field and displacements in bearingless induction motors," *IEEE Transactions on Industry Applications*, vol. 48, no. 1, pp. 124–131, 2011.

[27] H. Nian, Y. Quan, and J. Li, "Rotor displacement sensorless control strategy for pm type bearingless motor based on the parameter identification," in *2009 International Conference on Electrical Machines and Systems*. IEEE, 2009, pp. 1–5.

[28] Y. Hua and H. Zhu, "Rotor radial displacement sensorless control of bearingless permanent magnet synchronous motor based on mras and suspension force compensation," *ISA transactions*, vol. 103, pp. 306–318, 2020.

[29] P. Hermann, "A radial active magnetic bearing having a rotating drive," *London Patent*, vol. 1, no. 500, p. 809, 1974.

[30] A. Chiba, T. Fukao, O. Ichikawa, M. Oshima, M. Takemoto, and D. G. Dorrell, *Magnetic bearings and bearingless drives*. Elsevier, 2005.

[31] B. R. Teare, "Theory of hysteresis-motor torque," *Electrical Engineering*, vol. 59, no. 12, pp. 907–912, 1940.

[32] L. Zhou *et al.*, "Magnetically suspended reaction sphere with one-axis hysteresis drive," Ph.D. dissertation, Massachusetts Institute of Technology, 2014.

[33] K. Raggl, T. Nussbaumer, and J. W. Kolar, "Comparison of separated and combined winding concepts for bearingless centrifugal pumps," *J. Power Electron*, vol. 9, no. 2, pp. 243–258, 2009.

[34] Z. Fang, Z. Zhu, L. Wu, and Z. Xia, "Simple and accurate analytical estimation of slotting effect on magnet loss in fractional-slot surface-mounted pm machines," in *2012 XXth International Conference on Electrical Machines*. IEEE, 2012, pp. 464–470.

[35] A. E. Fitzgerald, C. Kingsley, S. D. Umans, and B. James, *Electric machinery*. McGraw-Hill New York, 2003, vol. 5.